Impact of water properties on the vertical distribution of light under sea ice

Master Thesis

in

**M. Sc. Climate Physics:
Meteorology and Physical Oceanography**

Christian-Albrechts-Universität Kiel

Hans JAKOB Belter
Matriculation number: 5686

Advisor: Prof. Dr. Katja Matthes
             [**GEOMAR**, Helmholtz-Zentrum für Ozeanforschung Kiel]
Co-advisor: Dr. Christian Katlein
             [**Alfred-Wegener-Institut**, Helmholtz-Zentrum für
             Polar-und Meeresforschung, Bremerhaven]

Kiel, July 2017

Contents

Nomenclature

Abbreviations

AOP	Apparent optical properties
AR5	Fifth Assessment Report of the Intergovernmental Panel on Climate Change
FRAM	Frontiers in Arctic Marine Monitoring
FYI	First-year ice
IOP	Inherent optical properties
IPCC	Intergovernmental Panel on Climate Change
ITP	Ice-Tethered Profiler
MYI	Multi-year ice
PAR	Photosynthetically active radiation
RAMSES	Hyperspectral radiometer (manufactured by TriOS Mess- und Datentechnik GmbH)
RAMSES-ARC	Hyperspectral radiance sensor (Advanced Radiance Collector)
RAMSES-ACC	Hyperspectral irradiance sensor (Advanced Cosine Collector)
ROV	Remotely Operated Vehicle
VIPER	Submersible **VI**S (visible range) **p**rocess spectrophotomet**er** (VIPER-G2, manufactured by TriOS Mess- und Datentechnik GmbH)

Symbols

A Absorbance ($[AU]$)

$c(\lambda)$ Spectral beam attenuation coefficient ($[m^{-1}]$)

F_λ Monochromatic flux density (irradiance, $[\mathrm{W}\,m^{-2}]$)

F_S Incoming shortwave irradiance ($[\mathrm{W}\,m^{-2}]$)

F_T Transmitted shortwave irradiance ($[\mathrm{W}\,m^{-2}]$)

I_0 Base intensity

I_λ Monochromatic intensity (radiance, $[\mathrm{W}\,m^{-2}\,sr^{-1}]$)

κ_{bb} Broadband extinction coefficient

           (integrated over the wavelength range from 320 to 950 nm, $[m^{-1}]$)

$\kappa(\lambda)$ Spectral extinction coefficient ($[m^{-1}]$)

κ_{PAR} PAR-integrated extinction coefficients (400 to 700 nm, $[m^{-1}]$)

λ Wavelength

ld Method using all data points within a layer of pre-defined thickness

           (3, 5, 8 or 10 m) for exponential fitting

nm Method using a number (3, 5, 8, 10) of consecutive data points for

           exponential fitting

T_{bb} Broadband transmittance

           (integrated over the wavelength range from 320 to 950 nm)

$T(\lambda)$ Spectral transmittance

T_{PAR} PAR-integrated transmittance (400 to 700 nm)

Abstract

The Arctic sea-ice cover has decreased considerably over the last 35 years. The decrease in sea-ice extent and thinning of the ice layer strongly impact the interactions between atmosphere and ocean. Light penetration into the upper ocean is becoming a major factor influencing the energy budget at the atmosphere-ocean interface in the Arctic. In order to quantify the impact of this additional energy input on the upper ocean this study investigates the optical properties of seawater underneath Arctic sea ice.

A newly-revised remotely operated vehicle (ROV) was used to obtain optical and bio-optical data along depth profiles underneath Arctic sea ice in autumn 2016. Two methods are developed to estimate broadband extinction coefficients from hyperspectral irradiance (RAMSES) data using an exponential decay model. Estimated broadband extinction coefficients are compared to fluorescence and backscatter data and extinction coefficients calculated from an extinction sensor (VIPER) that was also mounted to the ROV.

The accumulation of biological matter at the first few sampling sites shows increased extinction of radiant energy in the upper layers of the profile. With increasing depth broadband extinction coefficients decrease. Considerable data limitations and the inconsistency of the ROV profiles strongly obstruct the intended investigation. Therefore, this study provides a revised plan for the conduction of ROV depth profiles in the polar environment that will improve future data sets. These improvements potentially allow future studies to identify water layers with distinct optical properties and their transition zones more successfully.

Zusammenfassung

In den letzten 35 Jahren hat sich sowohl die Ausdehnung, als auch die Dicke des arktischen Meereises deutlich verringert. Der Rückgang beider Parameter beeinflusst maßgeblich die Wechselwirkungen zwischen der Atmosphäre und dem Ozean. Die zunehmende Lichtdurchlässigkeit des Meereises spielt dabei für die Energiebilanz an der Grenzschicht zwischen Atmosphäre und Ozean eine immer wichtigere Rolle. Um den Einfluss dieses ansteigenden Energieeintrags auf die oberflächennahen Ozeanschichten beschreiben und quantifizieren zu können, werden in der vorliegenden Arbeit die optischen Eigenschaften von Meerwasser unter arktischem Meereis untersucht.

Im Herbst 2016 wurde ein weiterentwickelter Tauchroboter (remotely operated vehicle, ROV) eingesetzt, um optische und bio-optische Messungen entlang von Tiefenprofilen unter dem arktischem Meereis durchzuführen. Diese Daten bilden die Basis für die vorliegende Arbeit. Zwei neuartige Methoden wurden entwickelt, um mithilfe einer abklingenden Exponentialfunktion Breitbandextinktionskoeffizienten der unterschiedlichen Wasserschichten zu bestimmen. Diese, auf der Basis von hyperspektralen Irradianzmessungen (RAMSES) bestimmten Breitbandextinktionskoeffizienten, werden zunächst mit den errechneten Extinktionskoeffizienten eines Extinktionssensors (VIPER) verglichen. Anschließend erfolgt der Vergleich mit Fluoreszenz-und Rückstrahlungsmessungen, die ebenfalls mit dem ROV vorgenommen wurden.

Die Diskussion dieser Arbeit zeigt, dass die Ansammlung von biologischer Materie nahe der Eis-Ozean-Grenzschicht für die erhöhte Abschwächung der einfallenden Solarenergie an den ersten Messstationen verantwortlich ist. Mit zunehmender Tiefe verringern sich diese Breitbandextinktionskoeffizienten. Die begrenzte Datenverfügbarkeit und die Unregelmäßigkeit der ROV-Tiefenprofile limitieren die geplante Untersuchung. Daher präsentiert die vorliegende Arbeit einen überarbeiteten Plan für die Durchführung von ROV-Tiefenprofilen in den Polarregionen. Die Optimierung der Messprofile, sowie die erwartete Verbesserung der Datensätze haben das Potenzial, die Bestimmung von Wasserschichten mit unterschiedlichen optischen Eigenschaften in Zukunft deutlich zu vereinfachen.

1. Introduction

The Earth's climate is a complicated and highly variable system consisting of five major components: atmosphere, ocean, cryosphere, pedosphere and biosphere. The complex interactions between these components are responsible for the current climatic conditions. Due to the variability within the individual climate components and current anthropogenic climate forcing, the entire system is subject to continuous change. This master's thesis focuses on one vastly changing component of the cryosphere and its immediate environment - Arctic sea ice.

1.1 The role of sea ice in the climate system

Sea ice covers less than 8% of the global ocean area in boreal winter (Vaughan et al., 2013). Despite its comparably small spatial expansion sea ice is a crucial parameter that interacts with the atmosphere and the ocean. In addition, it is a feature influencing the direct interaction between the atmosphere and the ocean. Sea ice insulates the relatively warm ocean surface and controls fluxes of heat, moisture and momentum across the atmosphere-ocean interface (Dieckmann and Hellmer, 2010).
Sea ice varies seasonally and occurs in the Arctic Ocean and the Southern Ocean around Antarctica. Arctic sea-ice extent ranges from about $6 \times 10^6 km^2$ in September to about $15 \times 10^6 km^2$ in March (Comiso and Nishio, 2008; Cavalieri and Parkinson, 2012; Vaughan et al., 2013). During the transition periods between minimum and maximum extent, the formation and melt of sea ice alter the density structure of the ocean surface layer. During the formation of sea ice, most of the dissolved salts from the freezing seawater are not integrated into the newly formed ice. The salinity of the upper ocean increases, which leads to unstable stratification in the surface ocean. The density increase in the surface layer favours mixing and convection. During the melt season this process is reversed. The proportion of freshwater in the surface ocean is enhanced, which leads to increased ocean stratification (Dieckmann and Hellmer, 2010; Perovich and Richter-Menge, 2009). These density changes combined with regional bathymetry contribute to the global thermohaline circulation (Brandon et al., 2010). Transport of sea ice due to wind and ocean currents acts as a redistribution mechanism of freshwater in the Arctic. Heat fluxes associated with the formation and melting of sea ice impact the ocean as well as the atmosphere.

1.1.1 Energy budget of sea ice

Periodic sea-ice melt and freeze-up are controlled by variations in surface temperature and incoming shortwave radiation. Sea ice is the major factor governing the energy budget at the atmosphere-ocean interface in the polar regions. Figure 1.1 illustrates the sea ice energy budget (Arndt, 2016; Perovich and Richter-Menge, 2009). Radiant fluxes are most dominant (Persson et al., 2002). The incoming solar radiation is strongly affected by the partitioning of incoming light at the ice surface. The outgoing longwave radiation is a
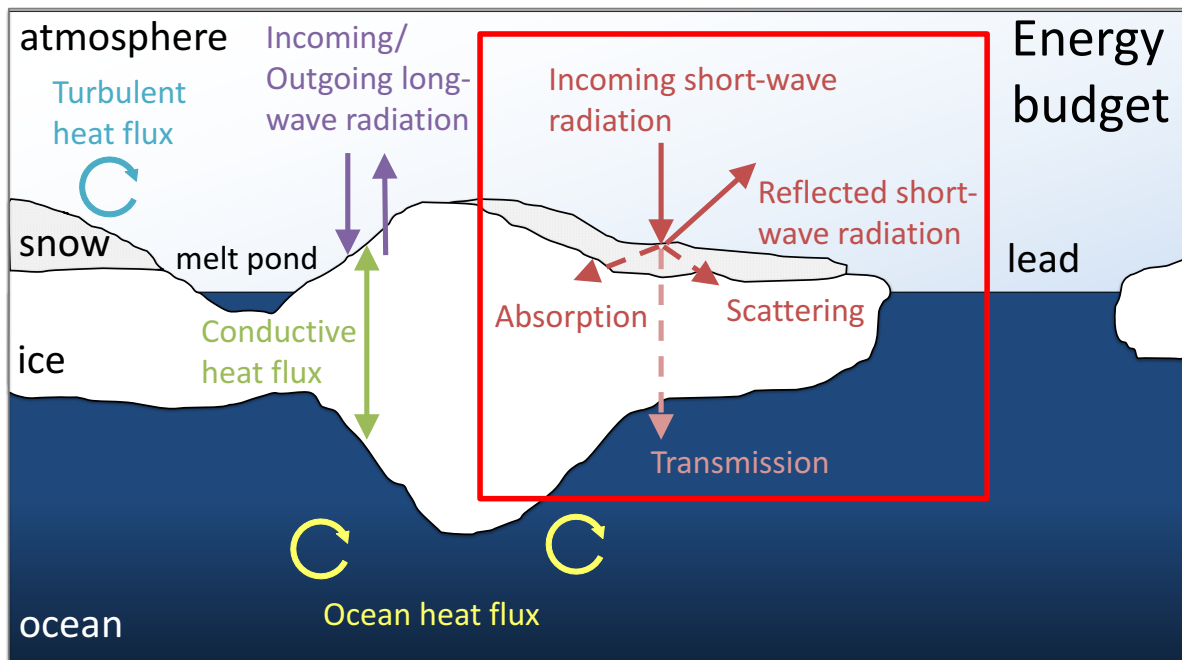
Figure 1.1: Schematic of the surface energy budget of sea ice (reproduced from Arndt (2016); Perovich and Richter-Menge (2009)). *Red* box indicates the shortwave solar radiation fluxes which this study focuses on.

function of surface temperature, while the incoming longwave radiation is determined by cloud cover (Perovich and Richter-Menge, 2009). Turbulent heat fluxes consist of latent and sensible heat fluxes. These fluxes are controlled through temperature and humidity differences between the atmosphere and the ocean, as well as the wind at the ice surface (Perovich and Richter-Menge, 2009). Finally, the under-ice heat budget is governed by the ocean heat flux, the heat that is conducted through the ice and the fraction of solar radiation that is transmitted through the ice into the ocean (Perovich and Richter-Menge, 2009). Thermal conductivity is dependent on the vertical temperature gradient between the ice surface and the ice bottom and the fraction of brine and air pockets in the ice layer (Perovich and Richter-Menge, 2009; Eicken et al., 2009). The fraction of incoming solar radiation that is transmitted to the ocean is controlled by the optical properties of the given ice cover and the spatial distribution of the ice floes. The availability of light underneath sea ice is crucial for the development of the under-ice ocean environment. In addition to heat input into the ocean that impacts the bottom melt of sea ice, solar incoming radiation transmitted through the ice layer favours biological activity and primary productivity (Nicolaus et al., 2010a,b). The knowledge about amount and spectral composition of this transmitted radiation is vital for biological studies (Eicken et al., 2009) and the understanding of the partitioning of incoming solar radiation in the under-ice ocean.

Sea ice is an extremely variable medium. Apart from temporal changes, sea-ice conditions vary on a variety of spatial scales (Nicolaus and Katlein, 2013). Figure 1.2 (S. Arndt, 2014)
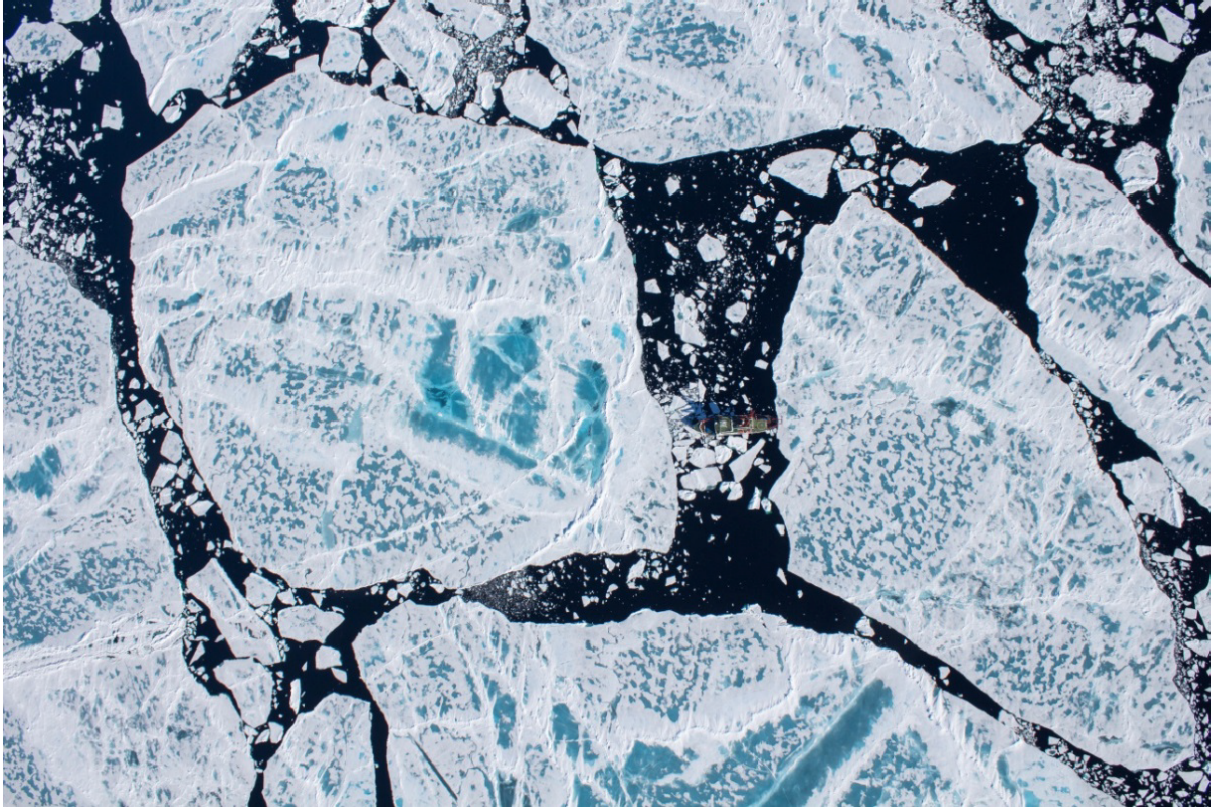
Figure 1.2: Aerial image of sea ice during the melt season 2014 (Image: S. Arndt).

provides a general idea of the heterogeneity of the sea-ice surface during the melt season. Spatial variability occurs both horizontally and vertically. Over horizontal distances from meters to hundreds of kilometers, sea-ice thickness can vary from $0\,\mathrm{m}$ (open water) to ridges of several meters (Perovich, 1996; Perovich and Richter-Menge, 2009; Nicolaus and Katlein, 2013). As a result of this spatial variability, the horizontal and vertical distribution of light under sea ice is extremely variable (Grenfell and Maykut, 1977; Nicolaus and Katlein, 2013).

The Intergovernmental Panel on Climate Change (IPCC) considers the cryosphere and its individual parts as a 'natural climate-meter' (IPCC, 2013). The number of processes associated with sea ice and its strong variability on temporal and spatial scales indicate the importance of sea ice for the climate system. Sea ice is responsive to important climate variables such as temperature, ocean currents and precipitation (Vaughan et al., 2013; Perovich and Richter-Menge, 2009). The impact of local sea-ice changes extends beyond the polar regions through the alteration of atmosphere and ocean circulations that are conveyed to the global scale (Brandon et al., 2010). Additionally, sea ice is an important participant in a number of positive and negative polar feedback mechanisms (Untersteiner, 1981), the most prominent one on a global scale being the ice-albedo feedback. Due to the large contrast in albedo between the open ocean and ice-/snow-covered ocean, the dark ocean surface absorbs more than 90% of the incoming solar radiation, while the latter
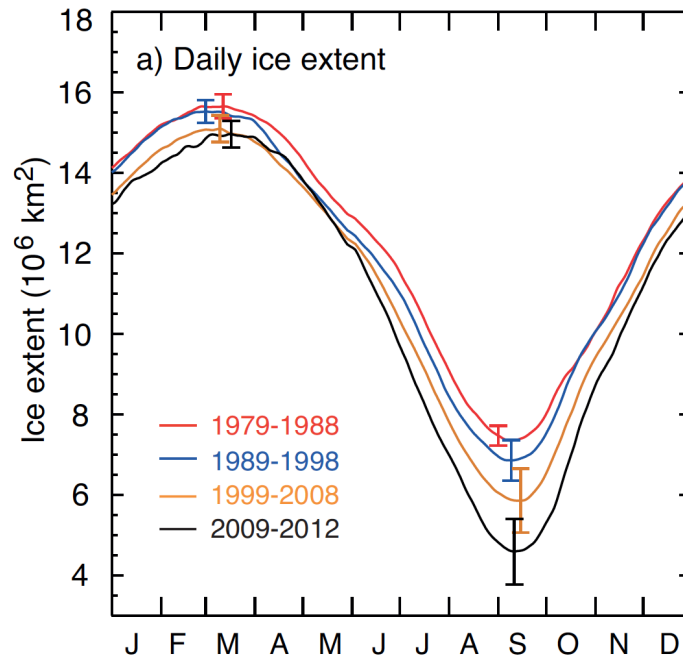
Figure 1.3: Decadal averages of daily sea-ice extent in the Arctic (1979 to 1988 in *red*, 1989 to 1998 in *blue*, 1999 to 2008 in *orange*) and a 4-year average daily sea-ice extent from 2009 to 2012 in *black* (Comiso, 2010). Values are derived from passive microwave data. Figure is taken from the IPCC (2013).

absorbs less than 30%. Hence, a decrease in sea-ice extent results in an increased amount of heat that is stored in the ocean. This additional energy further reduces the sea-ice cover, which in turn amplifies the warming of the ocean. This feedback is reversed in cases of strong cooling (Thomas and Dieckmann, 2010).

1.2 Current changes of Arctic sea ice related to climate change

Among natural variations in sea ice and the corresponding changing interactions with other climate components, the current situation indicates a significant response of Arctic sea ice to global climate change. When analysing the change in sea ice due to natural and anthropogenic forcing two parameters are considered predominantly.

First, sea-ice extent is defined as the sum of ice covered areas with ice concentrations of at least 15% (Vaughan et al., 2013). Sea-ice concentrations can also be calculated into total sea-ice area; however, both extent and area provide a general estimate of the horizontal dimension of the observed ice cover. With the advent of the satellite era (in 1979) continual daily coverage of the Arctic sea-ice extent has been realized (Vaughan et al., 2013). As Figure 1.3 (Vaughan et al., 2013) illustrates, over the course of the satellite era, Arctic sea-ice extent has decreased throughout all seasons. The most significant reductions of decadal mean sea-ice extent are evident during the sea-ice maximum in March
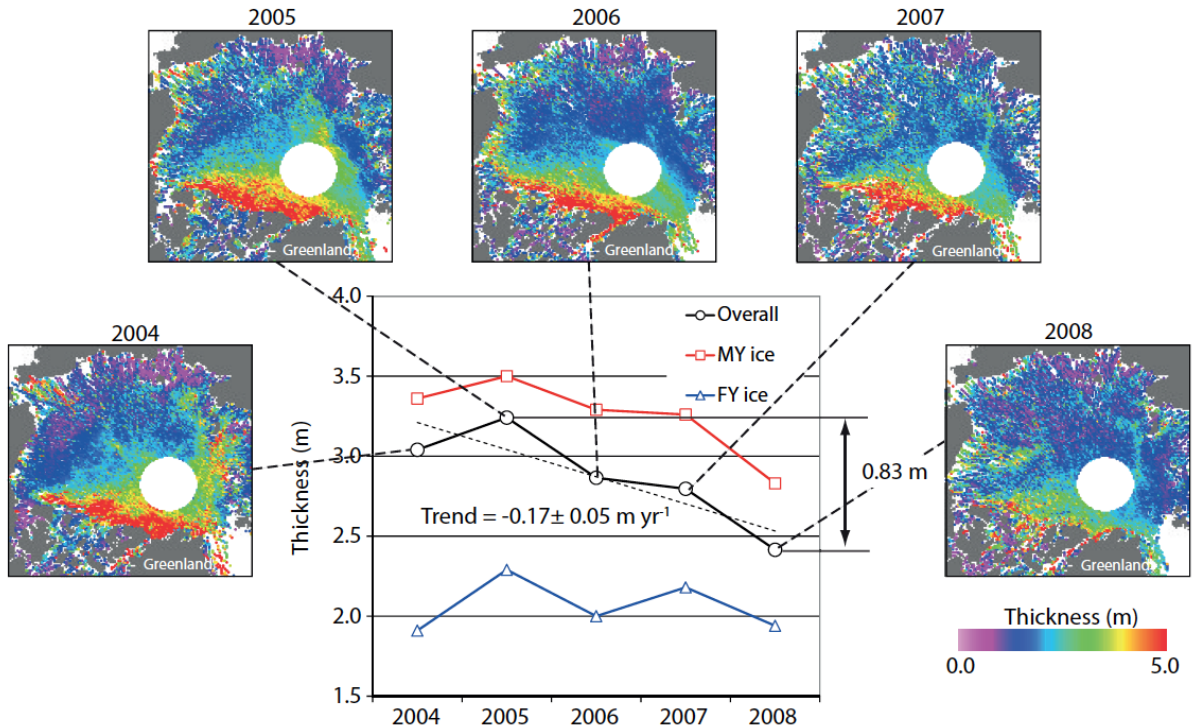
Figure 1.4: The distribution of winter sea-ice thickness in the Arctic and trends in average, first-year (FY) and multi-year (MY) ice thickness derived from ICESat data between 2004 and 2008 (Kwok and Rothrock, 2009). Figure is taken from the IPCC (2013).

and the sea-ice minimum in September. According to Vaughan et al. (2013), the total trend in Northern Hemisphere sea-ice extent between November 1978 and December 2012 is -3.8±0.3% per decade.

The second parameter vital for a meaningful discussion of sea-ice changes is the sea-ice thickness. Measuring sea-ice thickness is much more complex than measuring sea-ice concentration. A combination of submarine sonar, satellite altimetry and airborne electromagnetic sensing data sets provide strong evidence that Arctic sea-ice thickness has been decreasing in recent years (Vaughan et al., 2013). Among other factors, sea-ice thickness is related to the age of the ice. First-year ice (FYI) forms and melts within one annual cycle, while multi-year ice (MYI) is defined as ice that persisted throughout at least one melt season (Thomas and Dieckmann, 2010). Sea ice grows thicker through thermodynamic (strong temperature gradients between atmosphere and ice bottom) or dynamic (deformation) processes (Haas, 2010). While MYI is generally thicker ($> 2\,\mathrm{m}$ thickness) than FYI ($> 0.3\,\mathrm{m}$ thick), both ice types have different physical properties (Thomas and Dieckmann, 2010).

Arctic sea-ice thickness distribution is shown in Figure 1.4. The uneven distribution of ice thickness is a result of the prevailing drift and gyre regimes of the Arctic Ocean. While the Transpolar Drift Stream is responsible for ice export through the Fram Strait, sea ice is accumulated north of Greenland and the Canadian Archipelago due to the Beaufort Gyre (Perovich and Richter-Menge, 2009). Both, FYI and MYI show a negative trend

from 2004 to 2008 (Figure 1.4). The overall trend amounts to -0.17±0.05 m yr^{-1} (Kwok and Rothrock, 2009). Additionally, the percentage of thinner FYI has increased from 1983 to 2011 (Maslanik et al., 2007).

The overall decrease of Arctic sea-ice extent and thickness over the most recent years strongly affects the properties of sea ice and associated climate processes.

1.3 Motivation for this thesis

Sea ice is a major component of the Arctic climate system. It is variable on spatial and temporal scales and subject to significant reduction due to climate change. Numerous studies analysed the different optical properties that impact the sea-ice energy budget (Perovich, 1996). The special focus of these studies was on the interaction of sea ice with the shortwave radiative fluxes. Perovich (1996) investigated the reflection, extinction and transmission of light in relation to varying sea-ice properties. The development of more sophisticated measurement techniques allowed researchers to access sea ice from underneath. Subsequently, recent sea-ice research has expanded its scope to investigate the part of light that is transmitted through the ice in more detail. Nicolaus et al. (2012) and Nicolaus and Katlein (2013) proceeded to calculate optical properties of sea ice from under-ice measurements of transmittance. The aim of this study is to extend the analysis of the transmitted part of the light to the under-ice ocean layer and investigate the penetration of radiant energy within seawater.

Knowledge of light penetration into the ocean is of great importance in the context of global changes in climate. Incoming solar radiation is the most vital energy source and has implications not only for energy fluxes but also for biological activity which is the basis of the polar marine food web (Eicken et al., 2009; Katlein et al., 2015). Light transmission within the ocean strongly depends on the optical properties of seawater and its composition (Bricaud et al., 1995; Mobley et al., 2016). Taskjelle et al. (2016) found that increased under-ice phytoplankton bloom changes the optical properties of the ocean significantly. Increased bloom leads to a mean total absorption in the upper 20 m of the water column that is up to 4 times higher than prior to phytoplankton bloom (Taskjelle et al., 2016).
The under-ice light field in the Arctic Ocean is fundamentally different from the upper ocean light field in ice-free areas of the planet. This is due to the fact that the shortwave energy exchange is limited by the sea-ice cover (Grenfell and Maykut, 1977). The under-ice light field is irregular due to the heterogeneity of the ice cover, with the presence of leads, melt ponds, snow cover, ridges and different ice types (Petrich et al., 2012; Katlein et al., 2016; Laney et al., 2017). Sea ice shows varying optical properties that are non-uniformly distributed within the ice layer (Grenfell and Maykut, 1977). Optical properties are influenced by the inclusion of brine pockets, algae and sediments in the ice (Belzile et al., 2000; Laney et al., 2017). These factors lead to strong horizontal variations in the under-ice light field but they also vary in time generating temporal variability on scales of hours and longer (Laney et al., 2017). Additionally, sea-ice cover impacts the

vertical distribution of the light field in the underlying water column (Frey et al., 2011; Katlein et al., 2016; Laney et al., 2017). Only a fraction of the solar radiation is transmitted through the ice and into the ocean. This fraction is dependent on the season and the composition of ice and snow. With the decrease in Arctic sea-ice extent during the period from 1978 to 2012 and the strong thinning of the sea-ice cover following the summer minimum in 2007 (Vaughan et al., 2013), a larger fraction of the incident solar radiation is able to penetrate into the upper ocean (Nicolaus et al., 2012). This energy input is unprecedented and can potentially impact physical, biological and chemical properties of the Arctic Ocean. With the prospect of even more light penetrating the decreasing sea-ice cover, a more detailed understanding of the optical processes within the water column is required in order to assess the impact these changes have on the climate and eco-system. This thesis is an effort to complement model studies (Katlein et al., 2016) and point measurements of light in the water column below sea ice (Frey et al., 2011; Laney et al., 2017). Rather than analysing the water column as a whole, this study aims to identify optically different layers within the water column. Knowledge about these layers is important in order to understand the impact the increasing portion of light that is available to the upper ocean has on the ocean environment. Identifying these layers improves the understanding of where biological activity is most pronounced and where associated ocean heating takes place. With the prospect of future decrease in sea ice, the increased energy input has the potential to further amplify the sea-ice reduction and ultimately the Arctic warming (ice-albedo feedback).

All data used in this study was obtained using the newly-revised remotely operated vehicle (ROV) from the Alfred Wegener Institute, Helmholtz Centre for Polar and Marine Research (AWI). This sensor platform is equipped with a number of sensors for physical, chemical and biological oceanography as well as optical and acoustic sensors to provide a comprehensive account of the ice-water interface (Katlein et al., submitted).
Compared to typical under-ice point measurements like from Ice-Tethered Profilers (ITP) (Laney et al., 2017) or articulated extension arms (L-arm)(Light et al., 2008; Nicolaus et al., 2010b; Frey et al., 2011), the ROV provides the means to spatially distribute sea-ice and water measurements. Additionally, the measurements are less influenced by light pollution due to access holes, as the ROV access hole is always outside the designated sampling area. The ROV allows researchers to cover different parts of the selected ice floe and sample directly below various sea-ice types within one survey. This system also enables the research team to conduct depth profiles at freely selectable sites. Following Katlein et al. (submitted), this flexibility may help overcome the gap between point measurements and larger-scale ship, airborne and satellite surveys. Previous studies (Nicolaus et al., 2012; Nicolaus and Katlein, 2013) already utilized ROVs. However, the current ROV provides additional data sets to compare light measurements and to conduct interdisciplinary analyses of the ice floe and the water below.
Up until this thesis, the new ROV system has been used in the field only once, during the *RV Polarstern* expedition PS101 to the Arctic Ocean between September 9 and October 23, 2016. Therefore, this is the first time that the entire system was used within its designated work area, making the available data sets unique in their complexity but

also sensitive to errors. On the account that the new system has never been tested in the Arctic before, a second objective of this thesis is to understand the data sets obtained by this sensor platform and potentially improve the operating procedures of the ROV during depth profiles.

In summary the main objectives of this study are:

- the identification of water layers with different optical properties underneath sea ice

  - What happens to the increasing amount of light that penetrates sea ice?

- the understanding of the obtained data sets and the revision of the current operating procedures of the ROV during depth profiles.

2. Theoretical background

In order to lay the foundation for the following analysis of optical properties of seawater underneath sea ice, this chapter provides a short overview of the radiometric quantities (Liou, 2002) that are central to this study. In addition, important optical properties are described.

2.1 Basic radiometric quantities

The amount of radiant energy in a time interval and a specific wavelength interval is expressed in terms of area that it crosses and its direction. The direction is restricted to a differential solid angle (sterian [sr]), oriented at an angle to the normal of the area that is crossed. This quantity is referred to as the *monochromatic intensity* I_λ or *radiance* and is given in units of energy per area per time per wavelength per sterian ([W $m^{-2}\,sr^{-1}$]) (Liou, 2002; Eicken et al., 2009).

A second measure of the strength of electromagnetic radiation used in climate sciences is the *monochromatic flux density* F_λ or *irradiance*. Irradiance of radiant energy is given by the normal component of I_λ integrated over the entire hemisphere. F_λ is thus expressed in units of W m^{-2}. Integrating irradiance F_λ over the entire electromagnetic spectrum yields the total flux density (Liou, 2002).

2.2 Optical properties of sea ice and seawater

Light availability in the Arctic is governed by the seasonal cycle in solar insolation. In addition, the under-ice light field is controlled by the surface conditions and the properties of the prevailing ice types. Due to precipitation, melting and freezing, surface and ice conditions vary throughout the year.

Incoming shortwave radiation consists of a direct beam component and a diffuse component that occurs from the interaction of the direct light component with the atmosphere (Perovich, 1996). The total light reaching the atmosphere-ocean interface is partitioned at the ice surface. Part of it is reflected by the surface, a portion is absorbed in the ice and a last portion is transmitted through to the ocean (*red* box Figure 1.1). Relative sizes of these portions depend on the optical properties of the ice and on the wavelength of the incident light (Perovich, 1996). This study focuses the analysis on wavelength ranges from 320 to 950 nm and the photosynthetically active radiation (PAR, 400 to 700 nm) range. Optical properties are divided into two categories: inherent and apparent.

2.2.1 Inherent optical properties

Inherent optical properties (IOPs) are those properties that depend only upon the medium. They are independent of the ambient light field and are considered a material property (Mobley et al., 2016). There are two fundamental IOPs:

(i) Absorption refers to the loss of energy from electromagnetic radiation through an absorbing medium. It describes the ability of a medium to absorb incident radiation. The amount of absorption per unit length of the medium is given by the *absorption coefficient* (Sturm and Massom, 2010).

(ii) Scattering is a process by which particles in the path of an electromagnetic wave steadily extract energy from the incident wave and re-radiate that energy in all directions (Liou, 2002). The *scattering coefficient* provides the amount of scattering, while the *phase function* gives the angular distribution of scattered light (Sturm and Massom, 2010).

The combination of scattering and absorption is characterized by the *attenuation* or *extinction coefficient* (Sturm and Massom, 2010). Extinction coefficients are given in terms of path length (m^{-1}) (Liou, 2002).

2.2.2 Apparent optical properties

Apparent optical properties (AOPs) depend on the material properties of the medium (IOPs) as well as the composition of the ambient light field. In addition, they are required to display a sufficient amount of consistent material specific properties to be useful descriptors of the given medium (Mobley et al., 2016).

Two important AOPs for the investigation of sea ice and the underlying ocean are *albedo* and light *transmittance*. Albedo is the ratio between incident radiant energy that is reflected at the surface of a medium to the total incident radiant energy (Perovich, 1996; Sturm and Massom, 2010). Transmittance is the fraction of incident radiant energy that is transmitted through a medium (Perovich, 1996; Sturm and Massom, 2010). It is given as the ratio between transmitted radiation and total incoming radiation (Petrich and Eicken, 2010).

The presented investigation focuses on the optical properties of the ocean layer underneath Arctic sea ice. Therefore, this analysis limits its investigation to radiation that reaches the under-ice environment. This transmitted part is strongly dependent on the optical properties and distribution of sea ice. The partitioning of the light within the ocean layer depends on IOPs like, composition, morphology and concentration of particulate and dissolved substances in the water (Mobley et al., 2016) and the light field available at the bottom of the sea ice.

3.   Data and methods

The following chapter provides an overview of the Alfred Wegener Institutes remotely operated vehicle (ROV) system. This ROV was used for the first time during *RV Polarstern* cruise PS101 in autumn 2016. The system is equipped with multiple sensors for optical, oceanographic, and biological measurements and navigation under sea ice. Detailed descriptions of the ROV system, its sensors and the setup in the field are given in Katlein et al. (submitted) and will be summarized in Section 3.2. Later on, the newly-developed approaches to identify different ocean layers by means of their optical properties will be defined and explained.

3.1 PS101

The *RV Polarstern* cruise PS101 (KARASIK) took place from September 9 to October 23, 2016. One of the main objectives of the expedition was to investigate geological, geochemical and biological processes in the vicinity of sea mounts and hydrothermal vents in the Arctic Ocean. Furthermore, novel technologies were utilized to study Arctic sea-ice change in the scope of the 'Frontiers in Arctic Marine Monitoring' (FRAM) infrastructure program. The ROV, as one part of the FRAM program, was used at the PS101 ice stations (Boetius, 2017). Figure 3.1 displays part of the PS101 cruise track and all stations related to the FRAM program. Additionally, Table 3.1 provides a detailed overview of the ice stations conducted during PS101.

Table 3.1: Summary of all PS101 ice stations.

| Station number	PS101-057	PS101-096	PS101-114
Date	15 Sep. 2016	19 Sep. 2016	21 Sep. 2016
Latitude	85° 17.12' N	86° 48.66' N	86° 59.52' N
Longitude	060° 10.18' E	061° 36.57' E	057° 42.30' E
Dive time [h]	4.5	3.25	2.75
Dive distance [m]	1209	1158	1526
Station number	PS101-142	PS101-162	PS101-171
Date	26 Sep. 2016	29 Sep. 2016	01 Oct. 2016
Latitude	86° 50.53' N	86° 57.50' N	86° 51.54' N
Longitude	058° 12.59' E	056° 00.40' E	061° 43.50' E
Dive time [h]	3.5	3.5	1.75
Dive distance [m]	2384	2602	1210
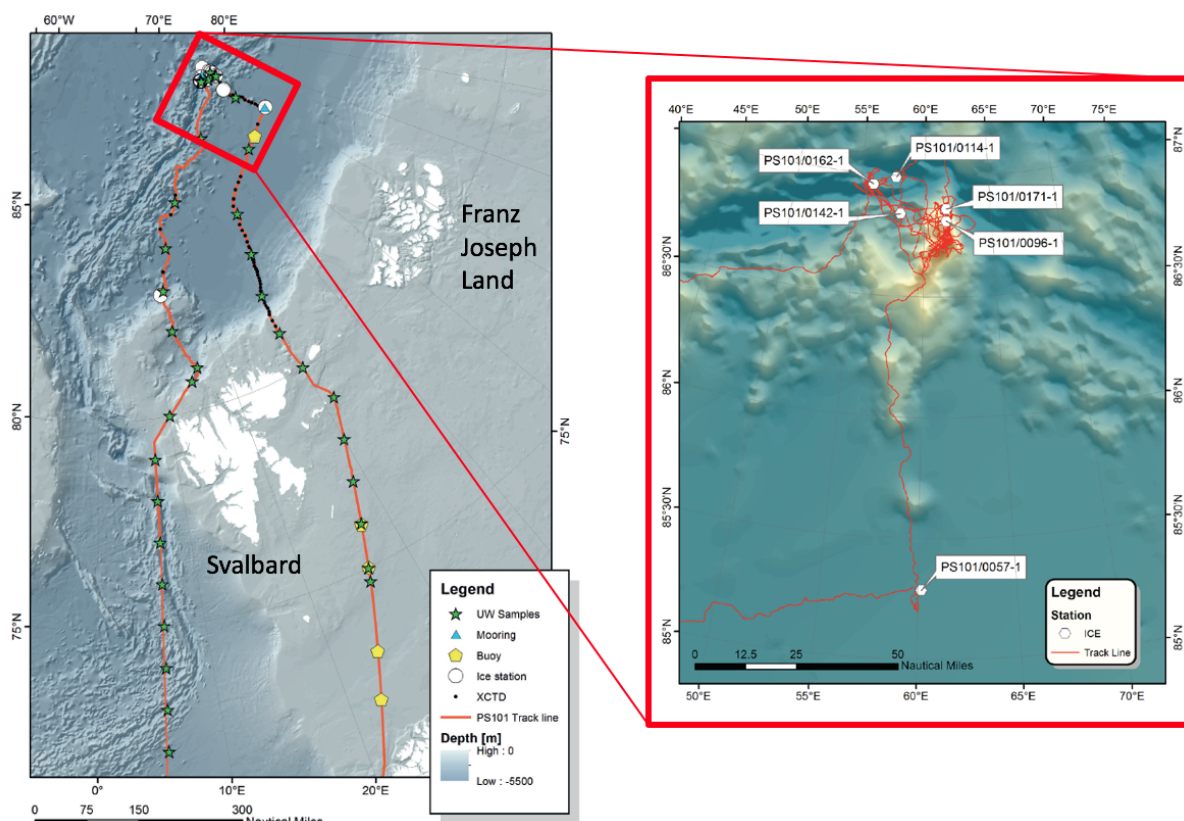
Figure 3.1: Segment of the *RV Polarstern* cruise track showing all stations within the FRAM infrastructure program during PS101 (Boetius, 2017). Excerpt shows a close-up of the ROV study area (adapted from C. Katlein). *White* dots indicate the ice stations.

3.2 ROV system

Direct field observations of Arctic and Antarctic sea ice are limited due to harsh climatic conditions and logistical difficulties in accessing these regions. One of the major challenges is to reach the under-side of the sea ice. Scuba diving is both limited in time due to cold temperatures, and limited air supply and extremely dangerous for the diver. A far lesser challenge is reaching the under-ice water layer with robotic vehicles. A wide variety of remotely operated and autonomous underwater vehicles can withstand the extreme conditions of the polar environment. The ROV used for this study has the advantage of being equipped with a comparably large number of different scientific sensors capable of tackling multiple tasks simultaneously. Usually, the development from single task systems towards comprehensive sensor platforms comes at the cost of vehicle handling, as platforms increase in size. This size increase is accompanied by an increased effort necessary to set up and operate the entire system. However, the presented system combines the substantial sensor suite of a larger vehicle with the logistical footprint of a much smaller one. This makes it the ideal tool for extensive interdisciplinary work with a small crew and a maximum preparation time on the ice of 2-3 hours.
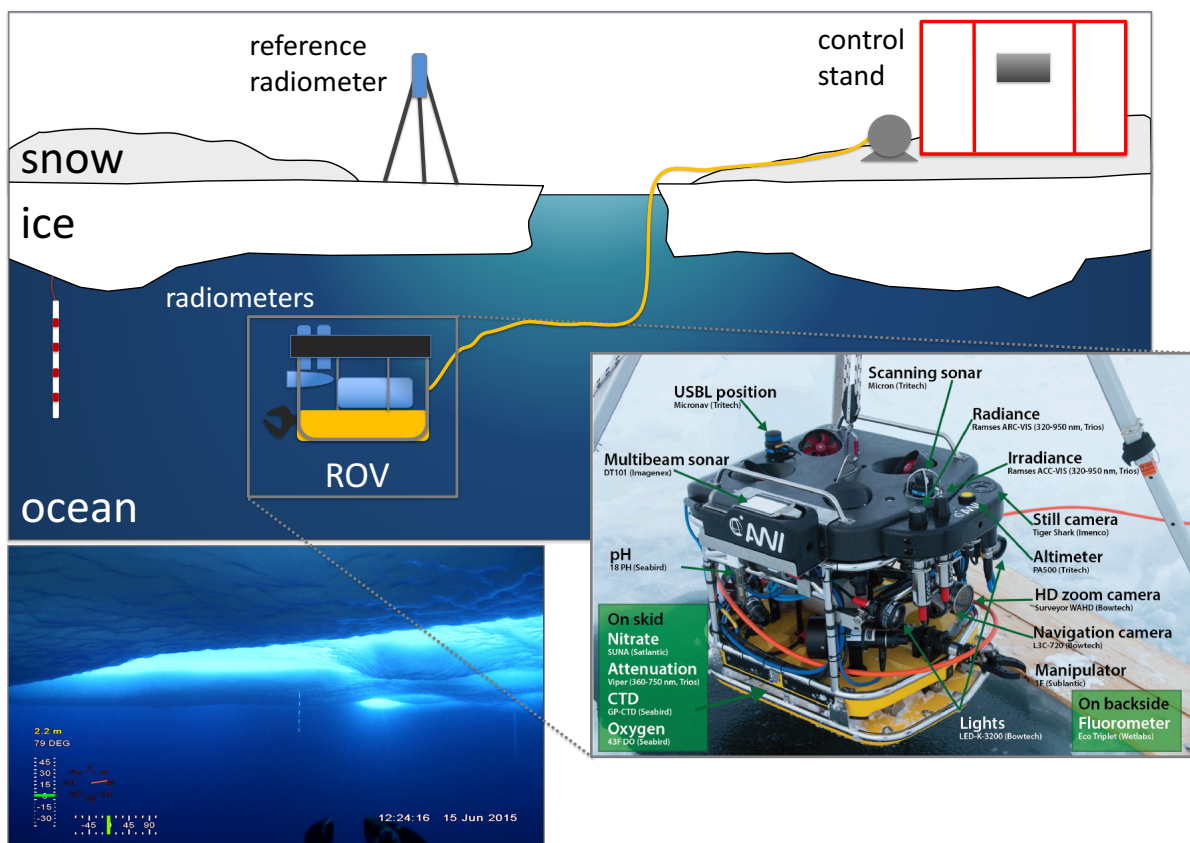
Figure 3.2: Schematic of the on-ice ROV setup (not true to scale). The extract displays the actual ROV and its sensors according to Katlein et al. (submitted). A picture of the under-ice situation during PS092 (2015) is shown on the bottom left.

3.2.1 Technical specifications and setup in the field

The ROV measures 0.73 m in height, 0.97 m in length, 0.75 m in width and has a maximum weight of 130 kg (including all scientific payload).The system is operated directly from the ice from a control stand (Figure 3.2). This small hut accommodates the computer system required to operate the ROV. The fully equipped control stand weighs approximately 750 kg and is lifted on the ice by crane and transported to the designated survey area by sledges. Once a suitable site is located, an access hole is prepared in order to lower the ROV into the water. In cases of thick ice or limited station time, the ROV can also be lowered into the water over the floe edge. However, a small hole as access point is preferable as it simplifies the deployment and minimizes unnecessary light pollution of the under-ice study area. Before starting the measurements, the survey area is prepared. Marker poles are installed under the ice along 50 to 100 m transects to simplify under-ice navigation (Figure 3.2). Arranging the marker poles is done with great caution in order to not disturb the ice and snow cover of the survey area. While the measurement setup and the control stand require a minimum sea-ice thickness of 0.3 m, the ROV is able to fly underneath much thinner ice during the transects. The ROV system provides a depth rating

of 500 m, while the 300 m fibre optic tether connecting the ROV with the control stand determines its maximum horizontal and vertical range. The scientific payload, however, is designed to withstand the conditions of the upper 100 m of the water column. Altogether, the system is mainly used in the upper 50 m of the water column as it is conceptualized to investigate interactions at the ice-ocean interface.

Managing the ROV and the associated equipment during an ice station in the Arctic requires a team of three scientists: one pilot in charge of the navigation of the ROV under the ice, a second pilot overseeing the scientific measurements during the survey and a third person outside the control stand, handling the tether and watching out for polar bears. Surveys are performed in a similar matter at every station. The ROV follows transects along the marked lines at a constant depth of 1-2 m (depending on ice thickness). The ROV covers the area in a lawn-mower like pattern and generally travels below its maximum velocity of 4 m/s (Figure 3.3a). This pattern and low ROV velocities ensure the best spatial resolution possible. Depending on the scientific objectives additional transects are conducted. In addition to the horizontal profiles close to the ice-ocean interface, similar transects are covered in deeper layers. If there is station time left, individual depth profiles are conducted (Figure 3.3b).

ROV depth profiles

The following analysis is based on the PS101 depth profile data. Before performing a depth profile dive, a weighted rope is lowered into the water through a small drill-hole. The rope provides additional support for the navigation of the system. In order to keep the ROV on track, the front camera is pointed towards the rope. The pilot can then follow the rope while descending the ROV. The main challenge is to prevent lateral motion of the ROV. An additional challenge is to maintain a constant ROV velocity throughout the cast. The profile length is dependent on light availability. The descent is continued until the rope is barely visible through the front camera. At that point the downcast is stopped and the ROV starts ascending for the upcast. Multiple factors can impact the profile dive and ultimately the retrieved data sets (Chapter 5.4). Single depth profiles were conducted at each of the six PS101 ice stations.

3.2.2 Optical sensor suite of the ROV

As Figure 3.2 indicates, the ROV is equipped with numerous scientific sensors, including multiple cameras, an USBL positioning system and a scanning sonar (for navigation purposes), a multibeam sonar system (for under-ice mapping), a Glider Payload CTD (GPCTD) and a pH sensor. For the purpose of this study, we will only focus on optical data retrieved from the ECO Fluorometer and Scattering sensor (ECO-Triplet), hyperspectral radiometers (RAMSES) and a hyperspectral transmissometer (Submersible VIS process spectrophotometer, VIPER-G2). RAMSES sensors as well as the VIPER extinction sensor were built by TriOS Mess- und Datentechnik GmbH (Rastede, Germany). The multibeam sonar system will be discussed by a parallel master's thesis by Veronica Coppolaro.
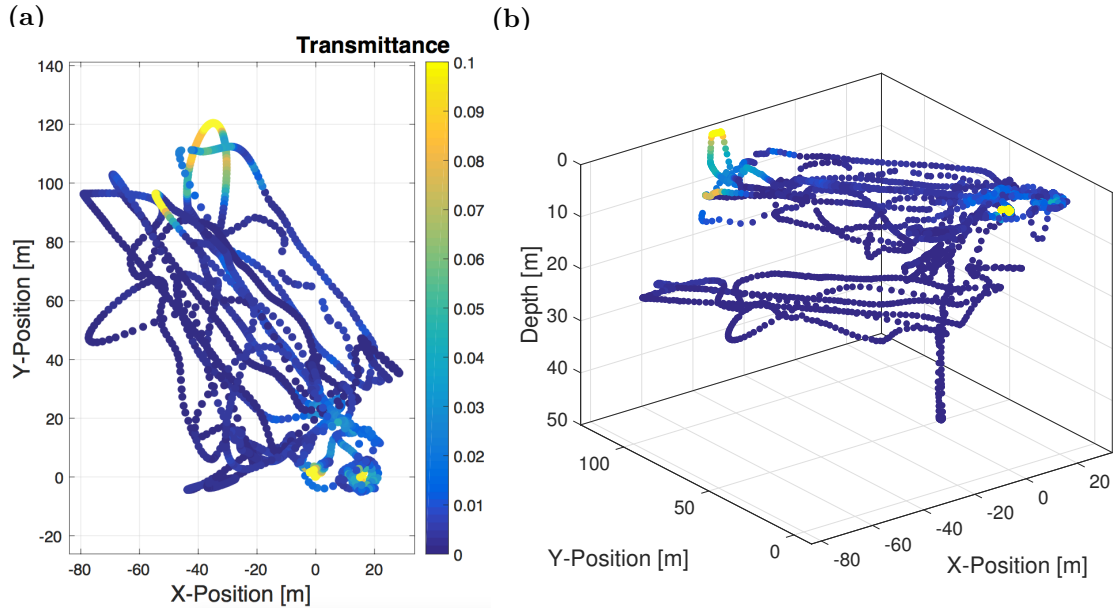
Figure 3.3: (a) shows a 2-D and (b) a 3-D map of broadband (320 to 950 nm) light transmittance of Arctic sea ice during station 162 of *RV Polarstern* expedition PS101 (North of Franz Joseph Land on September 29th, 2016). x-and y-positions are relative coordinates to the access hole on the chosen floe and indicate the survey track of the ROV.

Determining suitable measurement settings for the sensors in the polar environment is an ongoing process. Due to sensor malfunctions GPCTD data sets are especially unreliable for the analysis of upper ocean properties. The following section gives insight into the optical sensors utilized during the ROV depth profiles of PS101.

Spectral light fields transmitted through the sea ice were measured by two upward looking hyperspectral radiometers. The RAMSES-ACC (Advanced Cosine Collector) measures down-welling irradiance using a cosine collector plate. RAMSES-ACC measured irradiance is the primary parameter used for this study. In contrast, the RAMSES-ARC (Advanced Radiance Collector) measures radiance with a field of view of approximately 9°. An additional radiometer (RAMSES-ACC) is set up on the sea-ice surface to measure the incoming solar radiation (Figure 3.2). The on-ice irradiance sensor allows to calculate the transmittance (Chapter 2.2.2). All three radiometers measure wavelengths between 320-950 nm with a resolution of 3.3 nm. The accuracy of the radiometers is better than 6 to 10 %. The radiometers all use a measuring frequency of less than 8 s (burst mode, TriOS 2016).

Usually, the RAMSES sensors are inter-calibrated in order to ensure as accurate calculations as possible. Due to shipment difficulties and additional work by the manufacturer, the necessary experiments for the inter-calibration were not performed. Therefore, all calculations were done using the manufacturer's sensor calibration (TriOS), which is considered sufficient for the purpose of this study.

To complement and correct the under-ice RAMSES measurements, the ROV carried a hy-
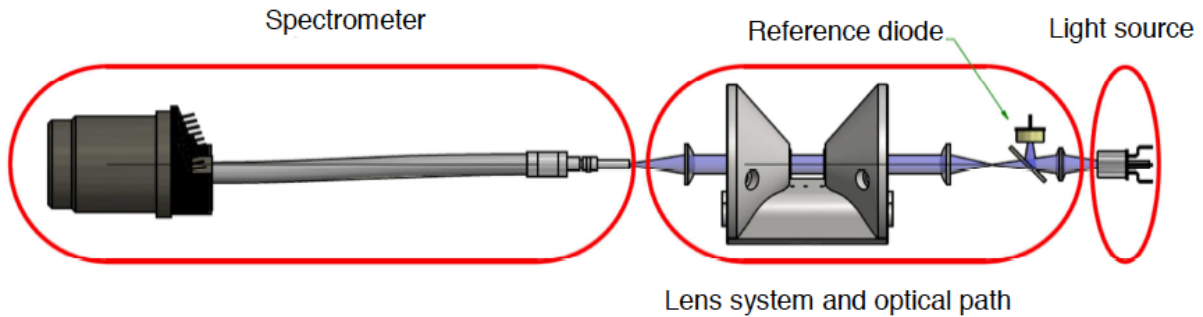
Figure 3.4: Schematic of the measurement arrangement of the VIPER-G2 (TriOS, preliminary manual).

perspectral extinction sensor (Submersible VIS process spectrophotometer, VIPER-G2), here referred to as VIPER. The VIPER records absorbance spectra in the visible range (360-750 nm) at a resolution better than 3 nm (TriOS, preliminary manual). Figure 3.4 illustrates the VIPER measurement arrangement. While the RAMSES sensors measure the downwelling radiance and irradiance, the VIPER measures light emitted from its own source. Five LEDs emit a focused light beam. After passing through the measurement medium (Arctic seawater in this case) along a pre-defined path, the beam is focused at the inlet slit of a small spectrometer. As the emitted light is absorbed and scattered by particles and molecules on its path through the medium, the spectrometer collects the remaining spectrally-resolved light. The intensity I is determined and divided by the so-called base intensity I_0. The base intensity is a reference intensity given by a VIPER measurement in ultra-pure water (without particles and determinants). Following the TriOS manual (TriOS, preliminary manual) intensity and base intensity are then used to determine the absorbance A (Equation 3.3). RAMSES radiometers and VIPER do not measure the same light field. The RAMSES measures downwelling irradiance, which is dependent on the available under-ice light field, while the VIPER measurements provide absorbance spectra that are independent of the under-ice light field. The optical path length of the VIPER usually depends on the sampled medium. Highly contaminated media are sampled using a very short path length, while clean media are sampled with a longer optical path length. There are four path lengths available for the VIPER: 0.05 m, 0.1 m, 0.15 m and 0.25 m. As Arctic seawater is very clear, a path length of 0.15 m was selected for PS101. This configuration allows to measure a minimum of 0.3% and a maximum of 97.7% of the total intensity emitted by the LEDs. The interval between individual measurements is greater than 1 min (TriOS, preliminary manual). The measurement interval is strongly impacted by the conditions in the field, especially the heat generation of the LED light source (personal communication with Karin Munderloh, TriOS Support Team). The time stamps of individual measurements show variations in the measurement interval of 1 to up to 3.5 min for consecutive measurements. Depending on the temperature of the LEDs, the device takes extra time to cool before starting the next measurement. The measurement itself takes up to 20 s, consisting of a light and dark measurement (maximum 10 s each). The integration time for these measurements
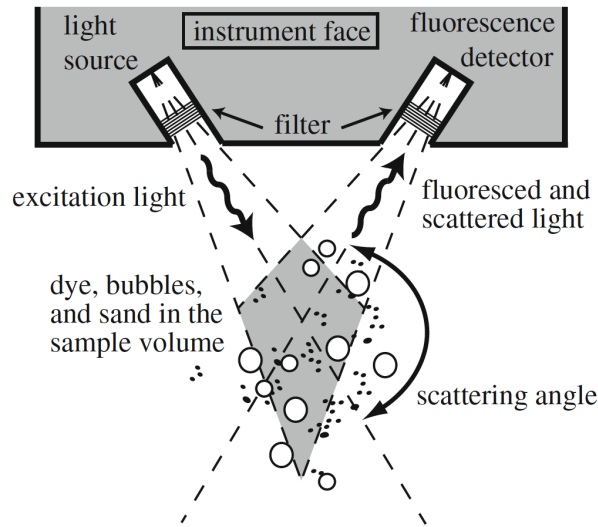
Figure 3.5: Schematic measurement arrangement of the ECO-Triplet (Clark et al., 2009).

is dependent on the availability of light, where samples with less light require a longer integration time (personal communication with Karin Munderloh, TriOS Support Team).

The third device used for the identification of water layers with distinct properties is an Environmental Characterization Optics (ECO) instrument produced by WETLabs. It provides three optical sensors (Triplet) with a user-defined configuration to measure scattering and fluorescence simultaneously (WETLabs, Manual 2016). The ECO-Triplet emits light at a specific wavelength and detects the fluorescence and backscatter of the medium at a certain angle (Figure 3.5). The output parameters given by the ROV's ECO-Triplet (ECO-Puck BBFL2-SSC) for the given setup are: Chlorophyll concentration ($[\mu g/L]$) measured at 695 nm, Fluorescent Dissolved Organic Matter (FDOM, $[ppb]$) at 460 nm and Scattering ($[m^{-1}]$) at 700 nm. According to Clark et al. (2009), the wavelength at which light is emitted from the ECO-Triplet is selected close to the fluorescent excitation peak of the parameter that is studied. The ECO-Triplet mounted to the ROV uses a standard configuration for the detection of chlorophyll concentration and FDOM fluorescence (Laney et al. (2014), WETLabs data sheet). Backscatter wavelengths are set to a standard value within the PAR range (Laney et al. (2014), WETLabs data sheet) with regard to the clarity of Arctic sea water.

3.3 Methods

The subsequent section presents the different approaches developed for this thesis in order to identify water layers with different optical properties. RAMSES irradiance and VIPER data processing, as well as the methods to compare the data of the two sensors, will be explained. The data selected for this analysis is limited to the measurements taken during the depth profiles of the individual stations.
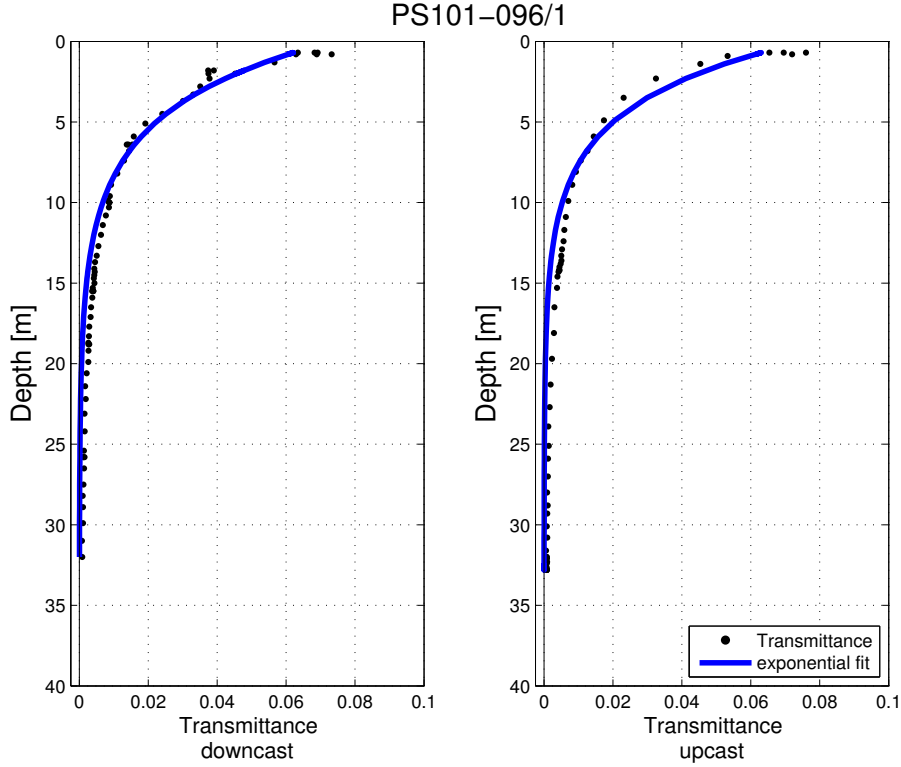
Figure 3.6: Broadband transmittance (*black* dots) calculated from RAMSES irradiance measurements at station PS101-096. *Blue* lines indicate the exponential fit for all depth profile data points following Equation 3.2. *Left*: downcast, *right*: upcast.

A depth profile consists of two different parts. The so-called downcast describes the descent of the ROV from the ice-ocean interface towards the maximum profile depth, while the ascent of the ROV back to the surface is called upcast. Ideally, both casts are conducted at the exact same spot and at a constant speed to avoid multiple recordings at the same depth.

3.3.1 RAMSES

Broadband extinction coefficient

Following Chapter 2.2, the broadband transmittance (T_{bb}, 320 to 950 nm) is calculated from on-ice and under-ice irradiance measurements according to the following equation (Perovich, 1996; Nicolaus et al., 2010b):

$$T_{bb}(t) = \frac{\int_{320}^{950} F_T(\lambda, t) d\lambda}{\int_{320}^{950} F_S(\lambda, t) d\lambda},$$
(3.1)

with F_S being the incoming shortwave irradiance measured by the on-ice radiometer and F_T the incoming shortwave irradiance transmitted through the ice. In this study, the integrated wavelength range of 320 to 950 nm is referred to as 'broadband'.

Broadband extinction coefficients κ_{bb} ($[m^{-1}]$) are estimated from Equation 3.1 by utilizing the exponential decay model previously used by Nicolaus and Katlein (2013):

$$T_{bb}(z) = T_{bb}(z_0) \cdot exp(-\kappa_{bb} \cdot z). \tag{3.2}$$

The broadband transmittance at depth (z) of the under-ice measurement is given by $T_{bb}(z)$, while $T_{bb}(z_0)$ is the broadband transmittance right below the ice-ocean interface. $T_{bb}(z_0)$ is the uppermost measurement of the respective cast and therefore selected as the starting value for the model. The advantage of this approach clearly is the simplicity of the model. The exponential decay model only takes into account (i) the broadband transmittance through the ice and (ii) the extinction coefficient of the seawater underneath the ice.

Frey et al. (2011) developed a more complex approach using an additional term to account for pond fraction and bare ice area. Their approach considers the spatial variation in light transmittance through sea ice due to varying ice types and different sea-ice surface properties. They showed that their model yields more reliable results during the melt season (June/July). However, the first ice station of PS101 took place after the 2016 Arctic sea-ice minimum, which was recorded on September 13, 2016 (AWI press release, September 2016). Melt ponds were only apparent on the floe of station PS101-057, while all other floes were consistently covered with snow (personal communication with Christian Katlein). Accordingly, the more complex approach by Frey et al. (2011) is not applicable to the situation that transpired during PS101.

In order to determine the broadband extinction coefficient, Equation 3.2 is used within the Matlab Curve Fitting Toolbox to fit an exponential function to the calculated broadband transmittance of each depth profile (Figure 3.6). Fitting all broadband transmittance data points of each depth profile, respectively, provides a single κ_{bb}-value per cast.

As one of the main objectives of this study is to increase the resolution and distinguish individual layers with different optical properties in the water column, multiple fits per profile are computed. This estimation of multiple broadband extinction coefficients per profile was done using two approaches:

- using a defined number of adjacent data points for fitting (nm-method)

- using all data points available within a layer of defined thickness (ld-method)

Independent of the selected method, it is important to have a sufficient number of data points available for the fitting process. For the specific purpose of finding layers with different optical properties, it is also necessary to obtain the finest vertical resolution possible. Therefore, the mentioned methods are applied with different scenarios in order to find the minimum amount of data points/layer thickness required for reliable extinction coefficients. Additionally, the different scenarios are selected with regard to finding changes in the water properties in layers as small as possible.

Number of data points: The first method of analysing distinct layers is to define a certain number of adjacent data points (nm) that are used for the fitting process. That method is divided into four scenarios. In each scenario, the value nm is set to either 3, 5, 8 or 10. That means the first 3, 5, 8 and 10 consecutive data points are selected for
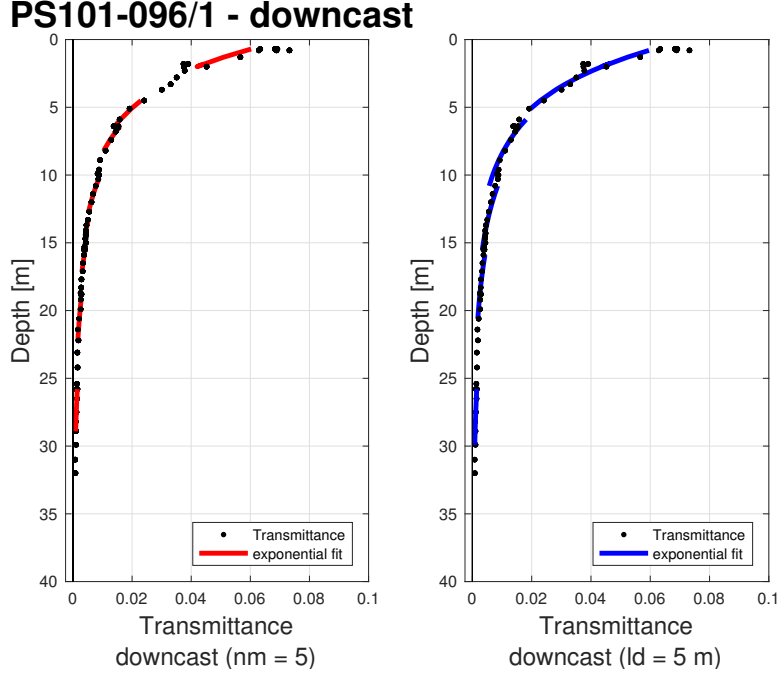
Figure 3.7: Broadband transmittance (*black* dots) calculated from RAMSES downcast measurements at station PS101-096. (a) *Red* lines indicate the exponential fits for the scenario *nm*5. (b) *Blue* lines give the exponential fits for all layers of 5 m thickness along the depth profiles (*ld*5) following Equation 3.2.

the fitting process before moving on to the next 3, 5, 8, 10 data points of the profile, respectively. This is done for all data points until the end of the profile. In the following the four scenarios are called *nm*3, *nm*5, *nm*8 and *nm*10.

Thickness of the layer: The second method utilizes all data points within a pre-defined layer of the thickness *ld* =3 m, 5 m, 8 m or 10 m. Now all data points within each of the 3, 5, 8 and 10 m thick layers are used for fitting the broadband transmittance values along the depth profile. Accordingly, the scenarios are called *ld*3, *ld*5, *ld*8 and *ld*10, respectively. Figure 3.7 displays the exponential fits projected on to broadband transmittance data for the scenarios *nm*5 (*left*) and *ld*5 (*right*). In order to determine the utility of the applied exponential decay model (Equation 3.2), the *coefficient of determination* R^2 is selected to compare the robustness of the results of the different scenarios of each method. Following von Storch and Zwiers (2003), R^2 is defined as the proportion of variance in the response variable that is explained by the fitted model. In other words, R^2 is the ratio between explained variability by the fit to total variability of the data. The maximum R^2 is one, which is equivalent to the statement that 100% of the data variability is explained by the fit. Contrary, its minimum is zero, expressing that the fit is not able to explain any of the variability of the given data. R^2 does not indicate how well the model fits in a statistical sense (von Storch and Zwiers, 2003).

Spectral extinction coefficient

Calculating spectral extinction coefficients for the RAMSES data along a depth profile is challenging. The presented fitting methods can be applied to the transmittance values of each wavelength. However, the results are dominated by noise at all depths. With the RAMSES data set obtained during the PS101 campaign, a rational calculation of spectral extinction coefficients along the depth profiles is not possible.

3.3.2 VIPER

Due to technical problems, VIPER measurements were only taken at four out of the six ice stations, and only two provide data for the depth profiles. This data limitation is one of the main challenges for the analysis and will be discussed extensively in Chapter 5. Accordingly, the comparison of VIPER and RAMSES measurements is restricted to stations PS101-114 and PS101-142. In the subsequent section, the processing algorithm applied to these two data sets is described.

Spectral beam attenuation coefficient

As stated in Section 3.2.2, VIPER output data is calculated using the ratio between measured intensity and base intensity. The final output are spectral values of absorbance A. The parameter with the unit AU (absorption units) is calculated according to TriOS (preliminary manual):

$$A(\lambda) = -log_{10}T(\lambda) = -log_{10}\frac{I(\lambda)}{I_0(\lambda)}, \tag{3.3}$$

with the spectral transmittance $T(\lambda)$, the incoming intensity $I(\lambda)$ measured by the spectrometer and the base-intensity $I_0(\lambda)$. In accordance, the spectral transmittance $T(\lambda)$ is given by:

$$T(\lambda) = 10^{-A(\lambda)} = \frac{I(\lambda)}{I_0(\lambda)}.$$

After calculating $T(\lambda)$ it is possible to compute the spectral beam attenuation coefficient $c(\lambda)$ ($[m^{-1}]$) given by Mobley et al. (2016) and Ramirez-Perez et al. (2014):

$$c(\lambda) = \frac{ln(T(\lambda))}{-r} = \frac{\left(\frac{I(\lambda)}{I_0(\lambda)}\right)}{-r}, \tag{3.4}$$

where r is the instrument path length, $0.15\,\text{m}$ in this study. The spectral beam attenuation coefficient calculated from VIPER absorbance values is independent of the ambient light field and therefore considered an inherent optical of the sampled water (Chapter 2.2.1). The analysis of VIPER attenuation coefficient spectra is limited to the photosynthetically active radiation wavelength range (PAR, 400-700 nm).

Broadband extinction coefficient

Prior to all integrations, the RAMSES and VIPER data sets are interpolated to the same wavelength grid from 400 to 700 nm with a resolution of 1 nm. Similar to the RAMSES broadband extinction coefficient values, the VIPER broadband values are not integrated over the entire spectrum but over a specific spectral range. In this case, broadband values are integrated over the 400 to 700 nm (PAR) range. Consistently, RAMSES broadband values that are used to compare the two measurement methods are integrated over the same spectral range.

The broadband extinction coefficients calculated from the RAMSES measurements are dependent on the incoming light field (AOP, Chapter 2.2.2). The spectral beam attenuation coefficient $c(\lambda)$, on the other hand, is a property specific to the respective medium, an inherent optical property. However, before the spectral beam attenuation coefficients are integrated, each spectral value calculated from the VIPER data is weighted by the amount of light (at each wavelength between 400 and 700 nm) available at the depth of the VIPER measurement. These light fields at each depth of the VIPER measurements are provided by the total irradiance values measured by the RAMSES sensor. The result is the PAR-integrated extinction coefficient κ_{PAR} from the VIPER absorbance data (AOP).

4. Results

This study focuses on the identification of water layers with distinct properties along depth profiles in the Arctic Ocean. The occurrence of those distinct properties can have multiple causes. Due to the limitations of taking in situ measurements in the extreme environment of the Arctic and the limited sensor suite of the ROV, only a few parameters are useful for determining these layers using the given data sets. The chosen approach uses optical data from RAMSES and VIPER measurements during PS101 to detect a reliable method (defined number of consecutive data points, nm, and layer of defined thickness, ld) and a suitable scenario to identify the characteristic water properties.

The following section presents the RAMSES results using the previously described multi-fitting approach from a few selected stations to compare the two methods and their scenarios. Secondly, PAR extinction coefficients κ_{PAR} computed from RAMSES and VIPER data are compared to investigate the performance of both devices. Lastly, spectral beam attenuation coefficients calculated from VIPER absorbance spectra are presented.

4.1 Broadband extinction coefficients

4.1.1 RAMSES

The first step towards identifying optical property changes along the vertical depth profiles requires the analysis of the utility of the selected model (Equation 3.2). First, broadband transmittance data is fit, using all data points of a profile, to prove the utility of the model. Following that, the model is used to fit multiple layers along the profile (Chapter 3.3).

As the approach of fitting a water column multiple times has not yet been applied in similar studies, the aim of this study is to find a model that proves reliable for the fitting of all profile data points and apply it to the multi-fit approach. Apart from the theoretical

Table 4.1: Broadband extinction coefficients $\kappa_{bb}([m^{-1}])$ estimated from the exponential decay model (Equation 3.2) for the up- and downcast of the depth profiles at each of the ice stations conducted during PS101. R^2 gives the coefficient of determination obtained for the broadband extinction coefficient κ_{bb} by the Matlab Curve Fitting Toolbox. *Bold* values indicate the two casts with R^2-values below 0.9.

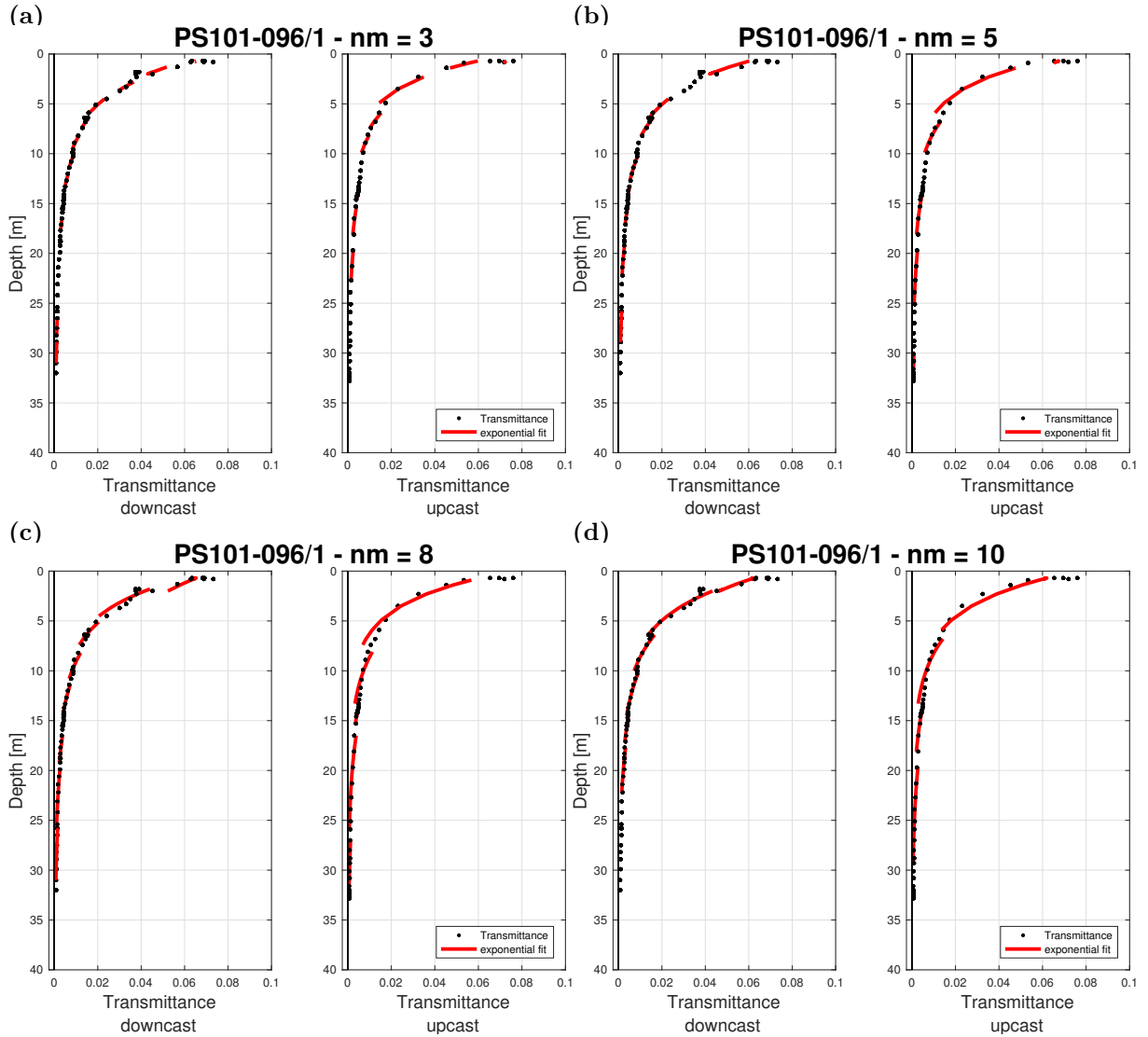|	PS101-057		PS101-114		PS101-162	
	downcast	upcast	downcast	upcast	downcast	upcast
$\kappa_{bb}([m^{-1}])$	0.1396	0.0836	0.1100	0.3760	0.2173	0.1505
R^2	0.9032	0.9152	0.9294	**0.8993**	0.9436	0.9482
	PS101-096		PS101-142		PS101-171	
	downcast	upcast	downcast	upcast	downcast	upcast
$\kappa_{bb}([m^{-1}])$	0.2378	0.2671	0.0694	0.0635	0.1283	0.3651
R^2	0.9732	0.9684	0.9350	0.9083	0.9303	**0.8133**

Figure 4.1: Multiple fitting approach using a predefined number of consecutive data points (*nm*) for each fit along the depth profile of station PS101-096. *Left* panels show calculated transmittance values (*black* dots) during the downcast, *right* panels during the upcast, respectively. *Red* lines indicate the exponential fits for the scenarios (a) *nm*3, (b) *nm*5, (c) *nm*8 and (d) *nm*10.

utility of the model described before, it is necessary to confirm the assumption, that the selected model is indeed sufficient for the purposes of this study.

Therefore, broadband extinction coefficients are estimated using all data points available from the depth profiles at the individual stations, resulting in one broadband extinction coefficient value for each cast at each station. Table 4.1 shows that, except for the results of two casts (*bold*), all coefficients of determination are larger than 0.9. The two exceptions still have values of $R^2 > 0.8$, which shows that the exponential decay model is suitable to explain a comparably high percentage of the total data variability. However, independent

of R^2-values, estimated broadband extinction coefficients show deviations between up-and downcasts at most stations. At PS101-162 for example, broadband extinction coefficients deviate by approximately $0.06\,m^{-1}$ between down-and upcast (0.2173 and $0.1505\ m^{-1}$) while their R^2-values indicate that almost 95% of the data variability is explained for each cast.

After establishing the model, the multiple fitting approach with the different scenarios (nm and ld) is performed for each cast of the PS101 depth profiles. In the following, two cases are presented that cover the most common results found in the collective data set.

Case study 1: station PS101-096

PS101-096 took place on September 19, 2016. The downcast (upcast) of the depth profile ranged from 0.8 to $32.0\,m$ (0.7 to $32.4\,m$). Downcast (upcast) broadband transmittance reached approximately 0.07 (0.075) at the beginning of the profile and decreased to approximately zero at $32.0\,m$ ($32.4\,m$)(Figure 4.1).

Number of data points nm
Figure 4.1 shows the exponential fits for the calculated broadband transmittance values using the different nm-scenarios. The individual panels suggest that the multiple fitting throughout the water column is possible independent of the nm-value. However, for every scenario the profile shows gaps where fitting was not possible. Gaps occur at the uppermost data points for every scenario and with increasing depth for all but the $nm8$-scenario. However, as the nm-value is increased and more adjacent data points are available for the fit in the deeper water layers, fitting yields results. In this example, only the $nm8$-scenario covers the entire depth range without gaps. Slight differences are also apparent between up-and downcast. However, Figure 4.1 shows whether the number of data points used for fitting was sufficiently large or too small. In contrast, the quality of the exponential fits as well as the broadband extinction coefficients can not be derived from Figure 4.1.

Figure 4.2 shows broadband extinction coefficients and R^2-values for the RAMSES transmittance data obtained by the nm-method. For the downcast a decrease in the broadband extinction coefficient is visible with increasing depth (Figure 4.2a). The computed values range from approximately 0.3 (within the upper $5\,m$ of the profile) to about $0.15\,m^{-1}$ at $30\,m$ depth. κ_{bb}-values are rather similar for the four nm-scenarios throughout the water column. Differences between the results of the different scenarios only occur in the upper $5\,m$ ($8\,m$) of the downcast (upcast). This is the part of the water column where broadband extinction coefficients peak, independent of the nm-scenario. Maximum values of the scenarios range from roughly 0.22 ($nm10$) to approx. $0.3\,m^{-1}$ ($nm8$) in this part. These results indicate a change in optical properties in the water column. κ_{bb}-values decrease with increasing depth.

R^2-values are displayed in the *middle* panel of Figure 4.2. For all scenarios, except $nm10$, R^2 values vary between 0.1 and 1 (Figure 4.2, *middle*). Low R^2-values are found in the upper $5\,m$ of the two casts and occasionally throughout the rest of the profile. This indicates that the high variability in the upper $8\,m$ visible in the broadband extinction coefficient data, likely is the consequence of poor fitting or strong broadband transmittance vari-
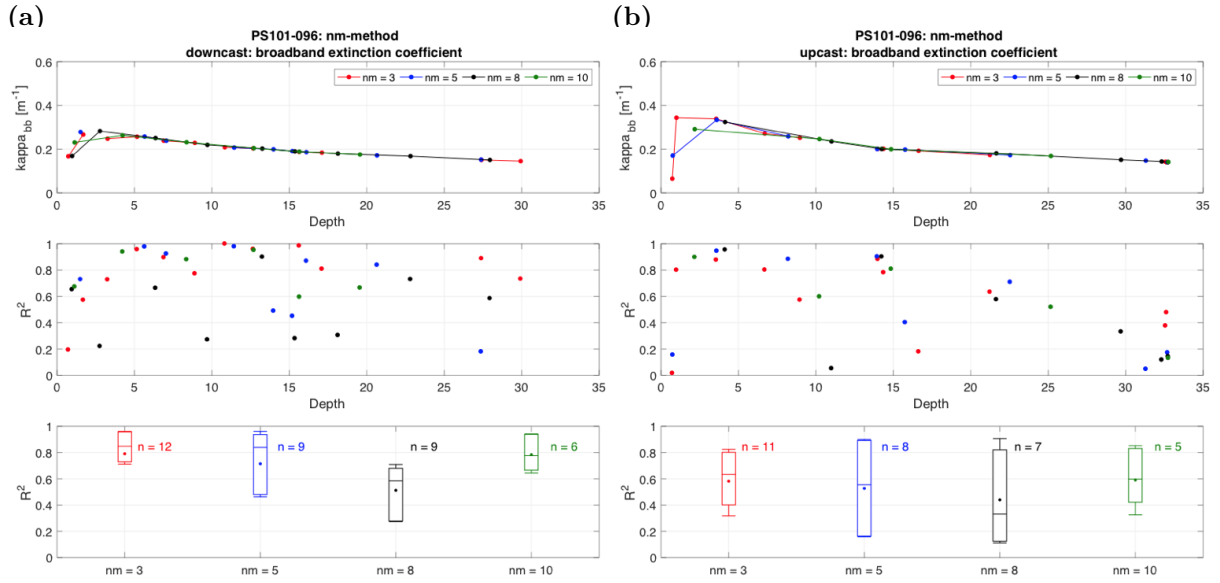
Figure 4.2: Fitting results for RAMSES broadband transmittance data from (a) down-and (b) upcast at station PS101-096. *Red* markers represent results from scenario *nm3*-fitting (*nm* =3), *blue* with *nm* =5, *black* with *nm* =8 and *green* with *nm* =10 (consistent color coding for all panels). The *top* panels display estimated broadband extinction coefficients κ_{bb} at the mean depth of the respective data points selected for the fitting process. The *middle* panels display the coefficients of determination R^2 estimated for every fit of each *nm*-scenario. The *bottom* panels display box plots of R^2 for the different *nm*-scenarios. Boxes are the first and third quartiles, while the whiskers show the 20th-and 80th-percentile. Dots indicate the mean, dashes the median. The number of coefficients estimated from fitting the entire water column (*n*) and used for the box plot is given next to the respective box.

ability along the profile. Therefore, these extinction coefficients need to be treated with caution.

The spread of the R^2-values is shown in the *bottom* panels of Figure 4.2. The downcast *nm3* R^2-values show the smallest spread between the first and third quartile (0.2), with highest mean (approx. 0.8) and median (approx. 0.85) values of all downcast scenarios. For this specific station and method, differences between up-and downcast are evident. Although, estimated broadband extinction coefficients below 10 m depth show a similar decrease to $0.15\,m^{-1}$ at maximum depth of the profile, the variability of κ_{bb} in the upper 8 m of the upcast is much larger than for the downcast. Values range from approx. 0.06 (*nm3*) to $0.35\,m^{-1}$ (*nm5*) in the upper 5 m. Accordingly, R^2-values differ much more strongly for the upcast. The mean and median of R^2 are lower for each *nm*-scenario during the upcast and the spread between the first and third quartiles is noticeably larger.

Thickness of the layer ld

Figure 4.3 shows the multi-fit approach using all data points within a predefined layer of thickness ld for the RAMSES broadband transmittance data of station PS101-096.
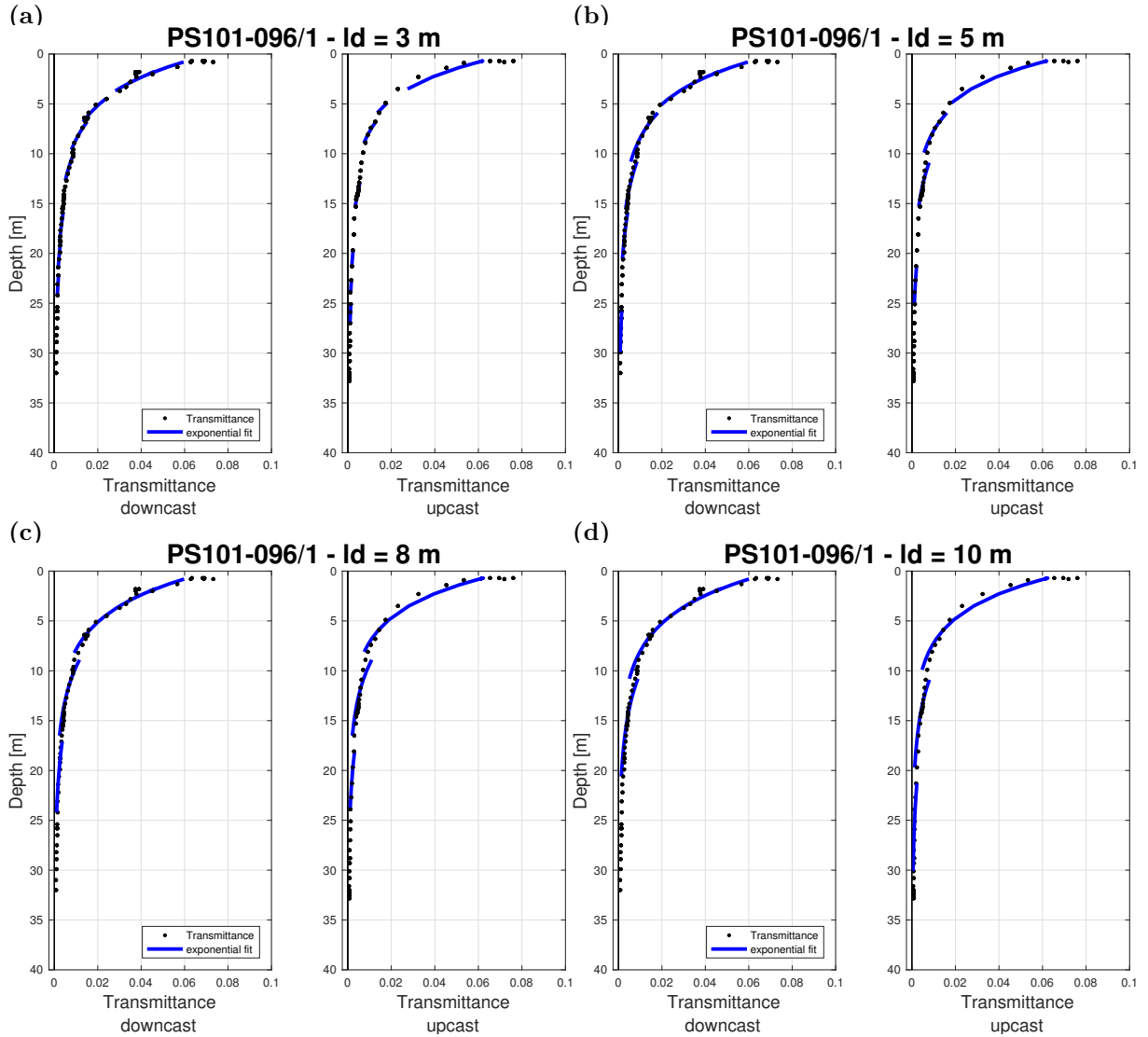
Figure 4.3: Multiple fitting approach using a predefined layer of the thickness (ld) for each fit along the depth profile of station PS101-096. *Left* panels show calculated transmittance values (*black* dots) during the downcast, *right* panels during the upcast, respectively. *Blue* lines indicate the exponential fits for the scenarios (a) $ld3$, (b) $ld5$, (c) $ld8$ and (d) $ld10$.

Similar to the nm-method fits, no fits are available for the uppermost data points of the profile. Additionally, no scenario is able to fit the data without gaps below 20 m.
The estimated broadband extinction coefficients and corresponding R^2-values for the ld-method are shown in Figure 4.4. Both up-and downcast show a decrease in broadband extinction coefficient from approx. $0.3\,m^{-1}$ in the upper 5 m to $0.15\,m^{-1}$ at 27 m depth. Values are very similar and upper layer variability and differences between the scenarios are not evident. This is confirmed by consistently high R^2-values in upper 15 m (13 m) of the downcast (upcast). R^2 is larger than 0.6 throughout the upper 13 m for all scenarios
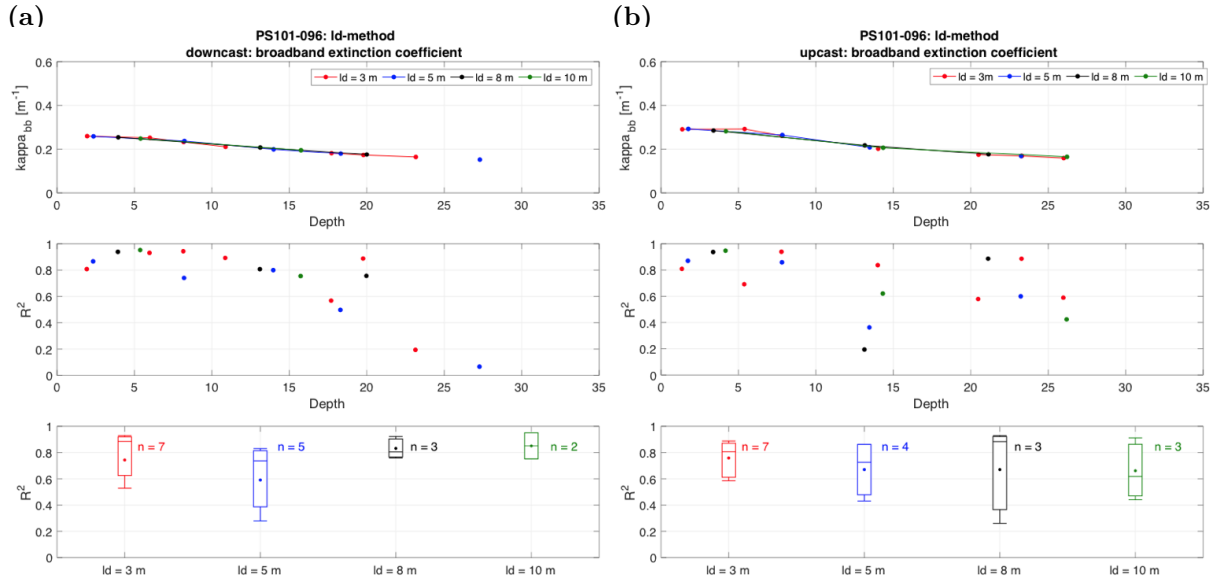
(a)

(b)

Figure 4.4: Fitting results for RAMSES broadband transmittance data from (a) down-and
(b) upcast at station PS101-096. *Red* markers represent results from scenario *ld*3-fitting
(*ld* =3 m), *blue* with *ld* =5 m, *black* with *ld* =8 m and *green* with *ld* =10 m (consistent
color coding for all panels). The *top* panels display estimated broadband extinction
coefficients κ_{bb} at the mean depth of the respective data points selected for the fitting
process. The *middle* panels display the coefficients of determination R^2 estimated for
every fit of each *ld*-scenario. The *bottom* panels display box plots of R^2 for the different
ld-scenarios. Boxes are the first and third quartiles, while the whiskers show the 20th-and
80th-percentile. Dots indicate the mean, dashes the median. The number of coefficients
estimated from fitting the entire water column (n) and used for the box plot is given
next to the respective box.

and both casts. Differences in R^2 between the two casts are more pronounced below 13 m.
Except for scenario *ld*5, the downcast R^2-values are larger and less dispersed than their
upcast counterparts (*middle* and *bottom* panels of Figure 4.4). For the *ld*3-scenario results
for the downcast, the spread between first and third quartiles of R^2 is approximately 0.3.
With increasing *ld* this spread decreases to 0.15 for *ld*8 and approximately 0.2 for *ld*10.
While the upcast R^2-spread between first and third quartile is similar to the downcast for
*ld*3, it increases to up to about 0.5 for *ld*8.
All in all, estimated broadband extinction coefficients are very similar for the four sce-
narios, although their associated R^2-values vary.

Summarizing, station PS101-096 results (Case 1) indicate a noticeable difference between
the two presented methods in the upper 5 m (downcast) and 8 m (upcast) of the profile.
While broadband extinction coefficients obtained using the *nm*-method vary by up to
approx. $0.1 \, m^{-1}$ ($0.29 \, m^{-1}$) for the downcast (upcast) in that upper part, no variation
between the scenarios is evident in the *ld*-method results at the same depth range. Dif-
ferences between up-and downcast are only visible in the R^2-values, which vary more for

the respective upcast results. Results from the four scenarios as well as up-and downcast findings agree very well when using the *ld*-method at this station.

Case study 2: station PS101-114

The second case study focuses on station PS101-114 (Case 2). As mentioned above, this is one of the stations where VIPER data was collected. The station took place September 21, 2016 and the downcast (upcast) depth profile ranged from 1.2 to 43.7 m (0.9 to 43.7 m). Broadband transmittance ranged from approx. 0.013 at the beginning of the downcast to close to 0 at maximum depth. Upcast broadband transmittance reached a maximum of 0.046 at 0.9 m depth and decreased towards 0 with depth. Different method and scenario fitting was less effective as for Case 1. Due to stronger broadband transmittance data variability throughout the two casts, fitting was more challenging. For both methods, fits are mainly available in the upper 20 m of the profile and show large gaps throughout the rest of the profile (see Appendix, Figure A.1 and Figure A.2).

Number of data points *nm*

Downcast broadband extinction coefficients for the four scenarios are available without gaps in the top 20 m. Below that only single ones (*nm*3 and *nm*8) occur between 30 and 35 m (Figure 4.5a, *top* panel). Extinction values are minimal in the the upper 5 m of the downcast. They range from approximately 0 (*nm*3) to roughly $0.1\,m^{-1}$ (*nm*8 and *nm*10). These minimal κ_{bb}-values are accompanied by comparably low R^2-values (ranging from close to 0 to approx. 0.7) for the same part of the profile (*middle* panel). Below 5 m, broadband extinction coefficients remain constant at approximately $0.15\,m^{-1}$ until values are no longer available. Between 3-13 m, R^2-values are above 0.75, indicating strong agreement between fit and broadband transmittance data. As the *bottom* panel shows,
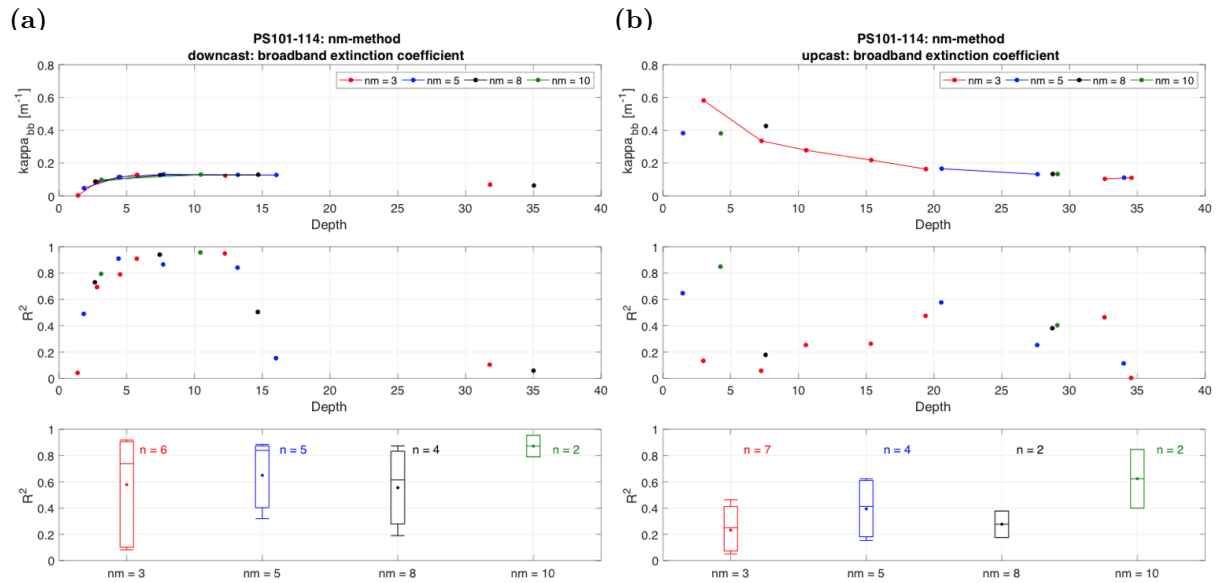
(a)　　　　　　　　　　　　　　　**(b)**

Figure 4.5: Same as Figure 4.2, but for results at station PS101-114.

29

R^2-values have noticeable spreads for $nm3$, $nm5$ and $nm8$. However, it is also apparent that the number of R^2-values available is limited ($n = 6$ for $nm3$ and $n = 2$ for $nm10$). The upcast estimates of κ_{bb} differ substantially from the downcast values and their corresponding R^2-values (Figure 4.5b). While $nm5$, $nm8$ and $nm10$ broadband extinction coefficients peak at about $0.4\,m^{-1}$ in the upper $10\,m$, $nm3$-scenario values reach their maximum close to $0.6\,m^{-1}$ at approximately $3\,m$ depth. The $nm3$-scenario is the only scenario with continuous fits in the upper $20\,m$. After the $nm3$-peak at $0.6\,m^{-1}$, broadband extinction coefficients decrease to just below $0.2\,m^{-1}$ at approximately $20\,m$. R^2-values are below 0.3 throughout that depth range with single exceptions for $nm5$ (0.65) and $nm10$ (0.85). Between 20 and $35\,m$, κ_{bb}-values for all scenarios are between 0.19 and $0.15\,m^{-1}$ and the corresponding R^2-values increase to between approximately 0.59 ($nm5$) and 0.4 ($nm10$).

Thickness of the layer ld
The ld-method results are similar to those employing the nm-method. Data limitations remain pronounced and differences between up-and downcast are evident (Figure 4.6). Downcast broadband extinction coefficients reach their minimum in the upper $5\,m$ and below $30\,m$ (approximately $0.07\,m^{-1}$). However, R^2-values indicate more reliable fits in the upper $15\,m$. Broadband extinction coefficients vary between approx 0.07 and $0.15\,m^{-1}$ in this upper layer, in which R^2-values exceed 0.6 for all scenarios. R^2-values drop below 0.4 for fits below $14\,m$ depth. Fits are very limited with, for example, only one $ld10$-scenario fit throughout the entire water column (depth range: 0.9 to $43.7\,m$).
Upcast fits are limited in number as are upcast fits for the nm-method. While broadband extinction coefficients below $15\,m$ depth correspond to R^2-values below 0.5, R^2-values above $15\,m$ depth suggest promising fits (Figure 4.6b). All scenarios show κ_{bb}-values of approximately $0.38\,m^{-1}$ with associated R^2-values between 0.65 ($ld3$) and 0.85 ($ld10$) in
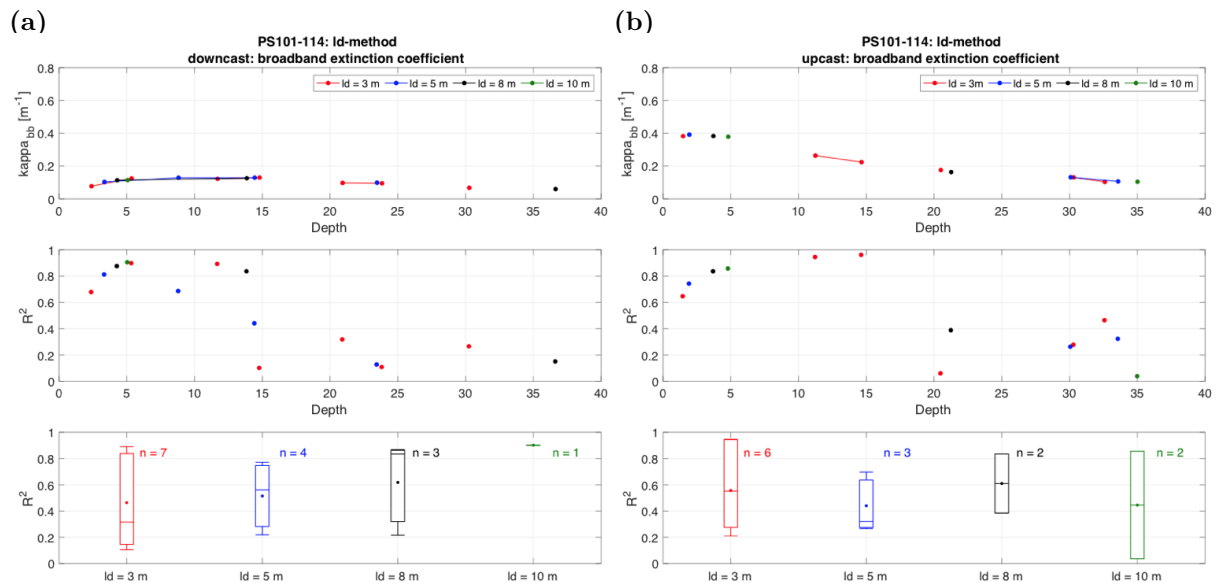

Figure 4.6: Same as Figure 4.4, but for station PS101-114.

the upper 5 m. Even though R^2-values for up-and downcast are similar for these upper 5 m of the water column, broadband extinction coefficients are significantly different. Upcast κ_{bb}-values reach up to approximately $0.38\,m^{-1}$, which is between 3.5 to 4 times as large as the downcast results show in this upper layer.

Summarizing, station PS101-114 (Case 2) estimations of broadband extinction coefficients are limited as fitting is not possible for most of the water column. Nevertheless, results indicate differences between up-and downcast, rather than between the two methods. Additionally, the figures reveal that high R^2-values can occur for significantly different extinction coefficients in the same layers of up-and downcast.

The two chosen cases are characteristic for all sampled stations of PS101. Case 1 indicates different broadband extinction coefficients in the upper 8 m of the water column as a result of the method selected for the analysis. Case 2, on the other hand, provides evidence that broadband extinction coefficient differences at station PS101-114 occurred between up-and downcast.

Even though the two cases represent the most common results for stations of PS101, their results are very different. Inspecting them separately is inadequate when conducting a method comparison. Furthermore, the number of fits of the individual stations alone is very limited. Therefore, analysing individual stations is not sufficient for a meaningful discussion about a superior method and scenario for the introduced fitting process. To account for the deficiencies of the single case studies, Chapter 5 proceeds to compare data from all stations of PS101 together.

4.1.2 RAMSES versus VIPER

The following analysis combines RAMSES and VIPER measurements obtained during stations PS101-114 and 142. These two stations are the only ones that provide VIPER data during the depth profiles. Unfortunately, data is sparse and unevenly distributed along the depth profiles. Figure 4.7 displays the RAMSES broadband transmittance values along the up-and downcasts of stations 114 and 142. Additionally, horizontal lines indicate where VIPER measurements were taken along the two casts. The lines indicate that only three VIPER measurements were taken per cast at station PS101-142. In contrast, the VIPER measured seven (five) times during the downcast (upcast) of station PS101-114.

In order to compare VIPER and RAMSES results, both data sets are interpolated to the same 400 to 700 nm (PAR) wavelength grid (1 nm resolution) prior to all calculations. Additionally, for the comparison of broadband extinction coefficients the spectral beam attenuation coefficients calculated from the VIPER absorbance data are weighted by the incoming light field (RAMSES), before the integration over the PAR wavelength range (Chapter 3.3.2).

The resulting broadband extinction coefficient values are shown for the *nm*-method (*ld*-method) in Figure 4.8 (Figure 4.9). PAR-integrated extinction coefficients estimated from the RAMSES data show similar differences between up-and downcast as the values integrated over the 320 to 950 nm wavelength range. Downcast values for both methods are
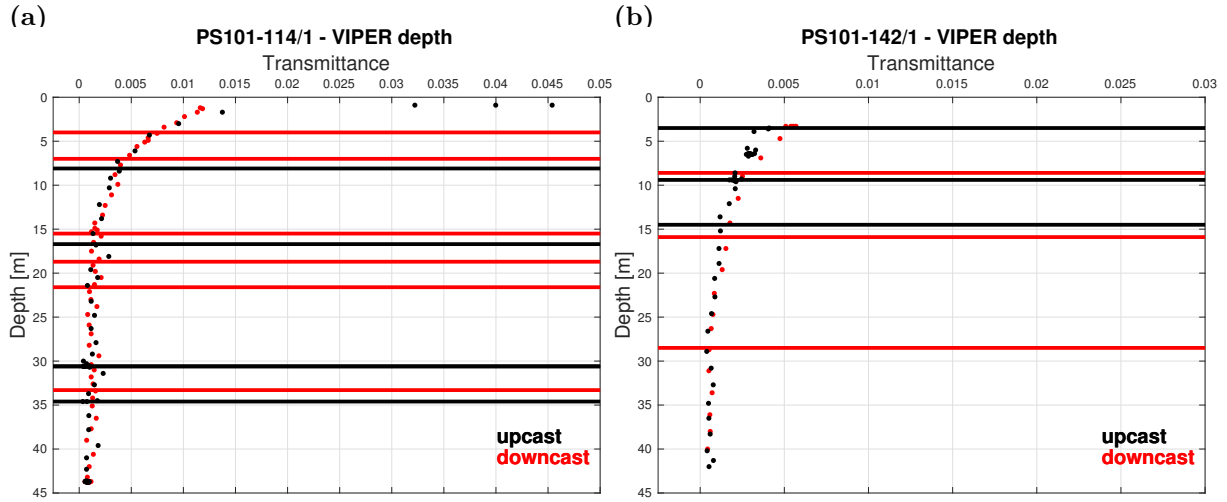
Figure 4.7: RAMSES broadband transmittance values (*dots*) along the depth profiles of (a) PS101-114 and (b) PS101-142. *Lines* indicate depths of the VIPER measurements. *Red* colours show downcast measurements, while *black* colours indicate the upcast.

minimal in the upper $5\,m$ of the profile and increase to a maximum of just below $0.15\,m^{-1}$ at approximately $15\,m$, before they decrease to approx. $0.1\,m^{-1}$ between 35 and $40\,m$ depth. Upcast RAMSES PAR extinction coefficients have a minimum of about $0.1\,m^{-1}$ between 35 and $40\,m$. Maxima for the *nm*-method are between approximately $0.4\,m^{-1}$ (*nm*3) and $0.27\,m^{-1}$ (*nm*8) at roughly 5 to $10\,m$ depth. The *ld*-method maxima are evident between 3 and $5\,m$ depth. Maxima are approximately $0.32\,m^{-1}$ for all scenarios.

Downcast RAMSES results indicate that the PAR extinction coefficient varies along the depth profile. However, values from all scenarios indicate that the PAR extinction coefficients lie below the detection minimum (*grey* line, $0.1535\,m^{-1}$) of the VIPER throughout the water column (Figure 4.8a, 4.9a).

VIPER PAR extinction coefficients vary noticeably along the downcast profile. Values range from approximately $0.29\,m^{-1}$ at $2\,m$ to approximately $0.01\,m^{-1}$ at roughly $22\,m$ and up to $0.28\,m^{-1}$ at $34\,m$ depth. Four out of seven values available along the profile are below the detection minimum of the VIPER.

Upcast RAMSES PAR extinction coefficients indicate a decrease in κ_{PAR} with depth (Figure 4.8b, 4.9b). VIPER values indicate the exact opposite. VIPER PAR extinction coefficients increase from approximately $0.05\,m^{-1}$ at $8\,m$ to roughly $0.78\,m^{-1}$ at $35\,m$ depth. Three of the five VIPER PAR extinction coefficients are below or at the detection minimum of the sensor.

PAR extinction coefficient results computed from RAMSES data at station PS101-142 show similar results for both casts and methods (see Appendix, Figure A.3). Minima (between 0 and $0.06\,m^{-1}$) of the different scenarios are evident above $10\,m$ of each cast. Values increase towards $10\,m$ depth and stay constant just below $0.1\,m^{-1}$ throughout the rest of the profile. κ_{PAR}-values calculated from VIPER absorbance data at that station are at least 4 times as large as those based on RAMSES broadband transmittance data. None of the VIPER values is below the detection minimum, but there is no apparent
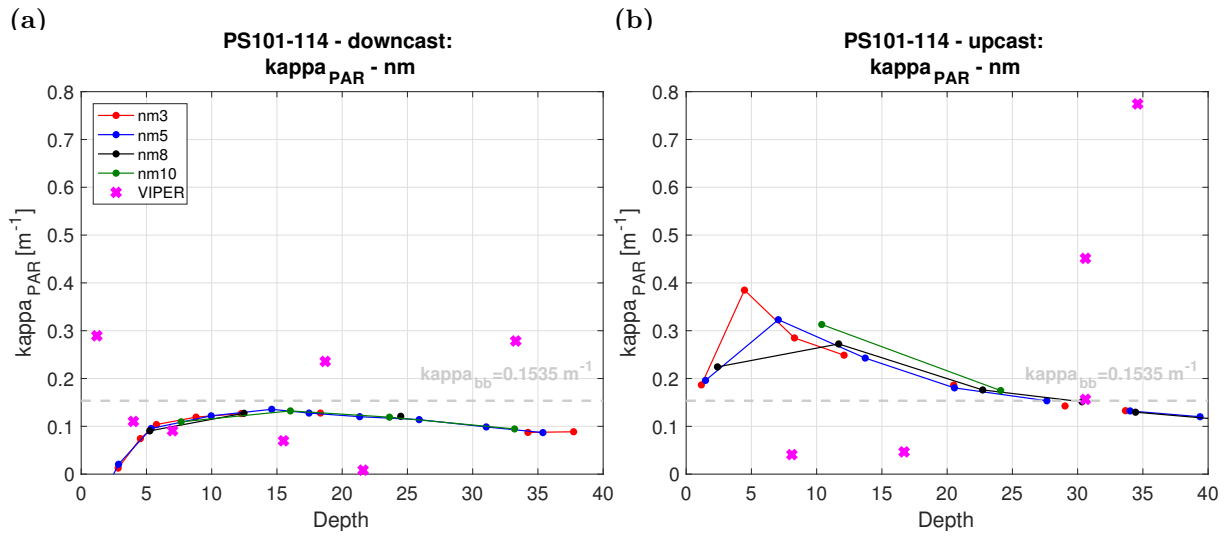
Figure 4.8: PAR extinction coefficients calculated from the RAMSES and VIPER (x-markers) data for (a) the downcast and (b) the upcast of station PS101-114. RAMSES PAR extinction coefficients are estimated using the *nm*-method. *Red* dots indicate the *nm*3-scenario, *blue* shows *nm*5, *black* the *nm*8 and *green* the *nm*10 results. The dotted *grey* line indicates the minimum broadband extinction coefficient detectable with the current VIPER setup (optical path length: 0.15 m).

Figure 4.9: PAR extinction coefficients calculated from the RAMSES and VIPER (x-markers) data for (a) the downcast and (b) the upcast of station PS101-114. RAMSES PAR extinction coefficients are estimated using the *ld*-method. *Red* dots indicate the *ld*3 scenario, *blue* shows *ld*5, *black* the *ld*8 and *green* the *ld*10 results. The dotted *grey* line indicates the minimum broadband extinction coefficient detectable with the current VIPER setup (optical path length: 0.15 m).
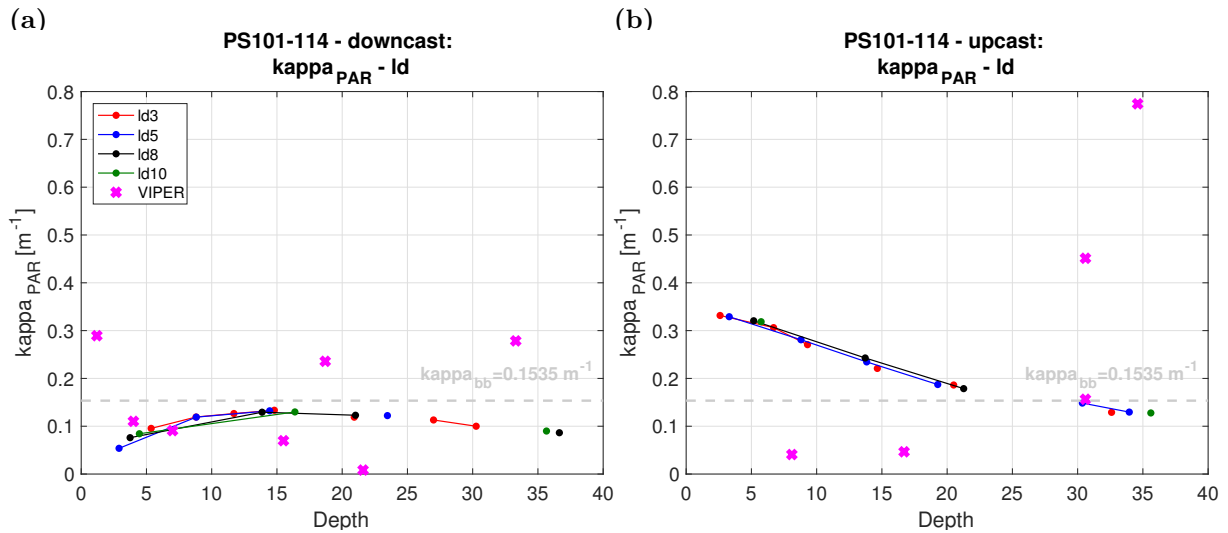
connection between the results of the two sensors.

Summarizing, VIPER PAR extinction coefficients are very sparse along the profiles of stations PS101-114 and PS101-142. They are unevenly distributed along the profiles and below the detection minimum of the VIPER in at least half the cases. There is no apparent connection between RAMSES and VIPER PAR extinction coefficients.

4.2 Spectral beam attenuation coefficients

The analysis of the wavelength-dependent beam attenuation coefficients is intended to determine the composition of the individual water layers. Spectral beam attenuation coefficients indicate the most important wavelength ranges for the extinction of light. Additionally, specific spectral patterns can provide information about the water properties as well as particle size and concentration at the sampled depth (Ramirez-Perez et al., 2014).

This spectral analysis is restricted to the data obtained by the VIPER. Useful estimates of spectral extinction coefficients from RAMSES transmittance data are confined to the upper few meters of the individual casts (not shown). Below that, noise dominates the data, making a meaningful comparison between VIPER and RAMSES values at depth impossible. Therefore, this section focuses on the spectral changes of optical properties along the depth profiles based on VIPER data only.

4.2.1 VIPER

PS101-114

Figure 4.10 shows (a) downcast and (b) upcast beam attenuation spectra obtained at station PS101-114. Most evidently, beam attenuation coefficients are below the detection minimum of the VIPER throughout the majority of the PAR-spectrum. Above $450\,nm$, up-and downcast values drop below $0.1\,m^{-1}$ at all depths and are dominated by noise for the rest of the PAR-spectrum. The downcast maxima for the beam attenuation coefficient are between 0.35 and $0.5\,m^{-1}$ at approximately $412\,nm$ (enlargement of Figure 4.10 a). Values drop between 0.2 and $0.1\,m^{-1}$ at approximately 420 nm. Between 430 and $450\,nm$, values fluctuate between 0.2 and $0.3\,m^{-1}$ at all depths. Beam attenuation coefficients at different depths indicate differences throughout the water column. The measurement closest to the ice bottom was taken at $4\,m$ depth. The corresponding spectral beam attenuation coefficients are the second largest between 400 and $450\,nm$. On the other hand, the deepest measurement was taken at $33.3\,m$ depth. The spectral values at this depth are noticeably higher between 400 and $450\,nm$ than the spectral values from all other depths. The smallest spectral beam attenuation coefficients in the first part of the PAR-spectrum (400 to $450\,nm$) are found at 18.7 and $21.6\,m$ depth. Differences between spectra from different depths are less pronounced at the slopes between local minima and maxima.

Upcast spectra between 400 and $450\,nm$ show a similar shape (enlargement Figure 4.10 b).
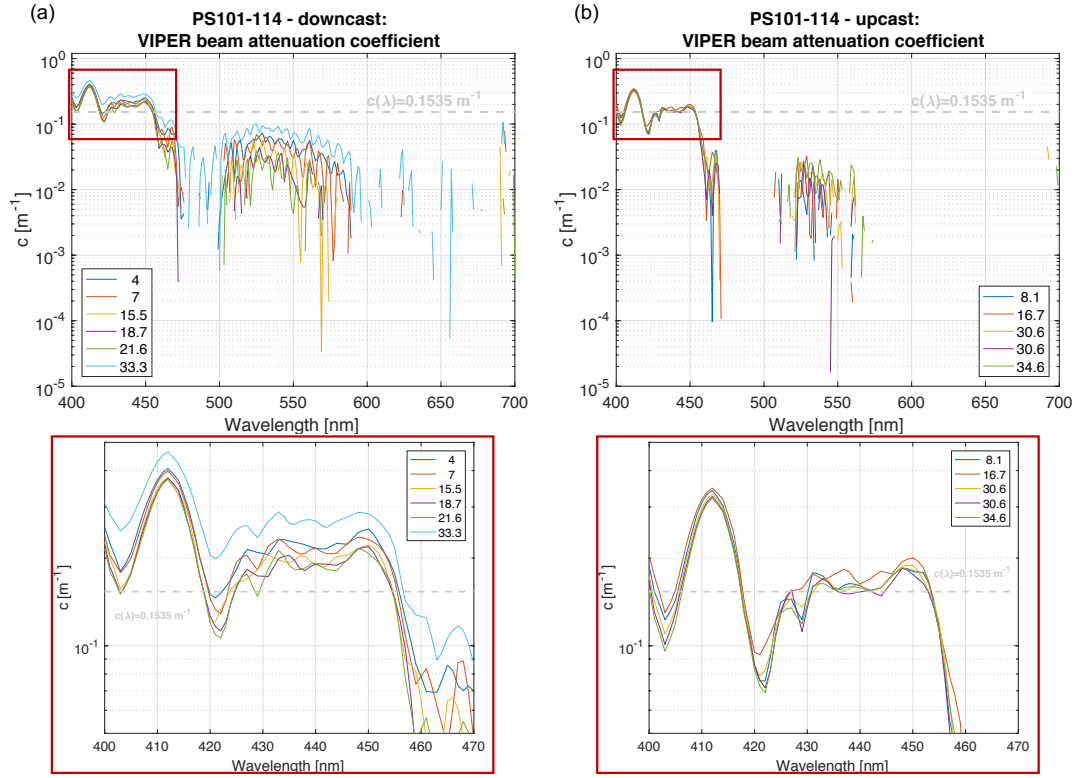
Figure 4.10: Spectral beam attenuation coefficients (400 to 700 nm, PAR) for the (a) downcast and (b) upcast of station PS101-114. Enlargements (*bottom* panels) show spectra in the wavelength range from 400 to 470 nm. Values are calculated from absorbance spectra obtained by the VIPER (Equation 3.4). Legend numbers indicate depths at which the VIPER measurements were taken ([m]).

However, spectra are only available for five depths along the upcast, and three of them were obtained between 30 and 34.6 m. The measurement closest to the ice-ocean interface was taken at 8.1 m depth.

Despite the fact that most of the measurements of the two casts were collected at different depths, the spectra at similar depths (downcast: 15.5 m, upcast: 16.7) show similar maximum values at 412 nm. Downcast values are higher at the local minima (approx. 403 and 422 nm). Largest spectral values are found at 16.7 m, while the smallest values are found below 30 m depth. As for the downcast, upcast spectra above 470 nm are dominated by noise and below the VIPER detection minimum.

PS101-142

Only three VIPER spectra are available per cast at station PS101-142 (Figure 4.11). In contrast to spectra at station PS101-114, the values in the PAR spectrum are above the detection minimum of the VIPER. Additionally, noise only dominates the data between 470 and 500 nm and above 600 to 650 nm. This is valid for both the up-and downcast. The downcast spectra are sampled at 8.6, 15.9 and 28.5 m depth (Figure 4.11a). The
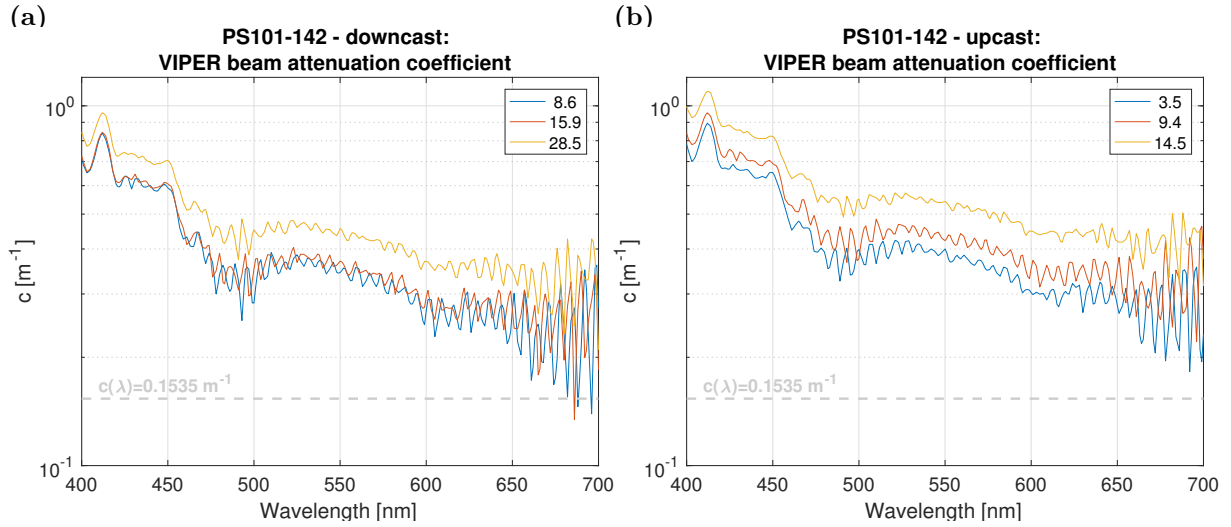
Figure 4.11: Same as Figure 4.10 but for beam attenuation spectra at station PS101-142.

maximum for each spectrum is reached at 412 nm. The maximum value for the upper two measurements is $0.85\,m^{-1}$, while the 28.5 m value reaches a beam attenuation coefficient of $0.94\,m^{-1}$. The 8.6 and 15.9 m coefficients take similar values, while the spectral beam attenuation coefficients measured deeper in the water column are approximately $0.1\,m^{-1}$ higher throughout the PAR-range. After rather constant values between 420 and 450 nm (approximately $0.6\,m^{-1}$ for 8.6 and 15.9 m and roughly $0.7\,m^{-1}$ for 28.5 m measurements) a distinct drop in the beam attenuation coefficients is evident. For all depths, this drop between 450 and 460 nm is of the approximate amplitude of $0.2\,m^{-1}$. For wavelengths above 460 nm, more variation is evident in all three spectra. Beam attenuation coefficients do not show peaks as sudden as for the wavelength range between 400 and 460 nm. Changes transpire over larger wavelength ranges (460 to 600 nm).

For the upcast (Figure 4.11b), spectra are available for 3.5, 9.4 and 14.5 m depth. An increase in beam attenuation coefficients with depth is evident along the entire PAR range. Differences between spectra at the individual depths are more distinct than for the downcast. Despite the fact that the general pattern of each spectrum is similar to the downcast results, individual beam attenuation coefficients are about $0.1\,m^{-1}$ larger for the upcast. The absolute maximum occurs at 412 nm with a beam attenuation coefficient value of approximately $1.1\,m^{-1}$ for the 14.5 m depth sample.

Summarizing, results from all but one cast (upcast PS101-114) indicate, that beam attenuation coefficients increase with depth. This increase is visible at all wavelengths within the PAR-range, that are not dominated by noise. The maximum peaks are at approximately 412 nm for spectra from all depths and casts. Spectral beam attenuation coefficients are very different between the two stations, but also between the two casts of each station individually. Noise is dominant between 470 and 500 nm and above 620 nm at station 142 and above 460 nm at station 114.

5.   Discussion

The following discussion aims at explaining the results found during the RAMSES case studies before proceeding to condense broadband extinction coefficient estimates from all stations into a detailed method and scenario comparison. Subsequently, PAR extinction coefficients calculated from RAMSES and VIPER data are investigated. In addition, beam attenuation coefficient spectra calculated from VIPER absorbance spectra are explained in order to determine property changes along the profiles, as well as to identify most optically active wavelength ranges. Furthermore, combining results from broadband, spectral extinction and beam attenuation coefficients as well as backscatter and chlorophyll concentration data allows to find actual changes in the optical properties of different water layers along the profiles of PS101. Finally, uncertainties and error sources are discussed.

5.1 Broadband extinction coefficients

5.1.1 RAMSES case studies

Case 1

The broadband extinction coefficient differences between the two methods for station PS101-096 data are limited to the upper $5\,\mathrm{m}$ (downcast) to $8\,\mathrm{m}$ (upcast) of the profile. The nm-method results show strong κ_{bb} variability in this layer, while no such variability is evident in the ld-method results. One reason for the variation in the nm-method in this part of the profile is likely the measurement itself. As evident in Figure 4.1, downcast transmittance data points accumulate multiple times within the upper $5\,\mathrm{m}$. For the nm-method this can result in a fit of consecutive points that are around the same depth and show a similar value. This leads to multiple use of a single data point for a fit, and thus, no reliable extinction coefficient can be obtained. This explanation is confirmed by low R^2-values for those specific broadband extinction coefficients. The most obvious example is provided by the $nm3$-scenario data (Figure 4.2). As the nm-value increases, this problem is reduced as more consecutive data points are available for the fit, masking the multi-sampling. While the downcast shows high frequency sampling with multi-sampling in the upper layer, the upcast was sampled less often and with changing frequencies. However, as the RAMSES sampling frequency was constant throughout both casts, the likely reason for the inconsistent sampling of the water column is a change in ROV velocity. It seems that, in the upper part of the downcast, the vertical velocity of the ROV was reduced to zero. Multi-sampling occurred and data points accumulated.

The same variability is not visible in the κ_{bb}-results obtained by the ld-method. When applying a fitting method that uses all data points within a layer of predefined thickness, multi-sampling within that layer leads to more data points used for the fit. Subsequently, the multi-sampling is masked and R^2-values for the fit are higher (Figure 4.4).

R^2 variations between up-and downcast can be explained by the the total dive times needed to complete the casts. The downcast dive time was exactly 06:00 min, while the upcast dive only took 04:56 min (31 m long depth profiles). The downcast is sampled more consistently and with smaller vertical distances between consecutive data points. The consistency in sampling the profile improved the fitting results of the downcast. The upcast profile is more variable and the PS101 ROV piloting team confirmed that the upcast was executed less carefully than the downcast.

For analysing transmittance data from this particular station, it is concluded that multiple fitting is possible but strongly influenced by multi-sampling. One measure to improve the analysis could be to exclude data points at positions where the ROV was not moving or combine the *ld*-and *nm*-method. The *ld*-method could be applied in parts of the profile where multi-sampling occurred, while the *nm*-method could be used for depth ranges that need higher resolution. Additionally, the casts need to be executed more carefully. Multi-sampling of single depths and large fluctuations in the vertical velocity of the ROV should be avoided. Apart from the upper 5 to 8 m of the two casts, the difference between the methods and their scenarios are negligible.

Case 2

Results from station PS101-114 indicate good agreement between the *ld*-and *nm*-method in the downcast. Low broadband extinction coefficients in the upper 5 m and corresponding small R^2-values suggest similar multi-sampling as seen in Case 1. Multi-sampling is confirmed by the depth-dependent transmittance analysis (Figure A.1). Data points taken during the downcast do not accumulate as strongly as for Case 1. Instead of pausing, the ROV moved very slowly, accumulating even more data points over a larger depth range by multi-sampling. Therefore, broadband extinction coefficients for *ld*3 and *ld*5 are influenced, which is confirmed by the R^2-values for those two scenarios in the upper 5 m of the profile (Figure 4.6). In general, the exponential decrease in light transmittance with depth is less constant than for Case 1. This is confirmed by the single-fit results presented in Table 4.1. The single-fits applied to station PS101-096 data are rather similar between up-and downcast (downcast: κ_{bb} =0.2378 m^{-1}, upcast: κ_{bb} =0.2671 m^{-1}), and approximately 97% of the transmittance variability is explained by the fit for each cast. In contrast, PS101-114 single-fits show different estimated broadband extinction coefficients between the casts (downcast: κ_{bb} =0.1100 m^{-1}, upcast: κ_{bb} =0.3760 m^{-1}), as well as lower R^2-values (downcast: $R^2 = 0.9294$, upcast: $R^2 = 0.8993$). It is possible that lateral movement of the ROV and strong currents influenced the ROV profile in Case 2. Horizontal movement of the ROV favours multi-sampling, but the broadband transmittance values can be influenced by the variability in the under-ice light field as well. As the under-ice picture in Figure 3.2 shows, the heterogeneity of the ice cover strongly impacts the distribution of light underneath it. Slight horizontal deviations from the vertical profile can lead to the sampling of a very different part of the light field. These influences lead to more data variability along the profile and, ultimately, poor or no fits. Although the dive time difference between the two casts was only 21 sec (upcast longer than downcast), fitting the upcast was more challenging. This is due to the strong broad-

band transmittance variability between consecutive data points. Very different broadband transmittance values at the top of the casts (approx. 0.012 at the top of the downcast and about 0.045 at the top of the upcast) also suggest the ROV ascended at a different spot and was measuring a slightly different water column and light field (Figure A.1). Another influencing factor is the selection process of the depth profile data. Depth profile data is selected from the overall ROV station data set manually. A slightly different selection can lead to entirely different fits of the profile, as the first and all consecutive starting data points for the fitting process are shifted.
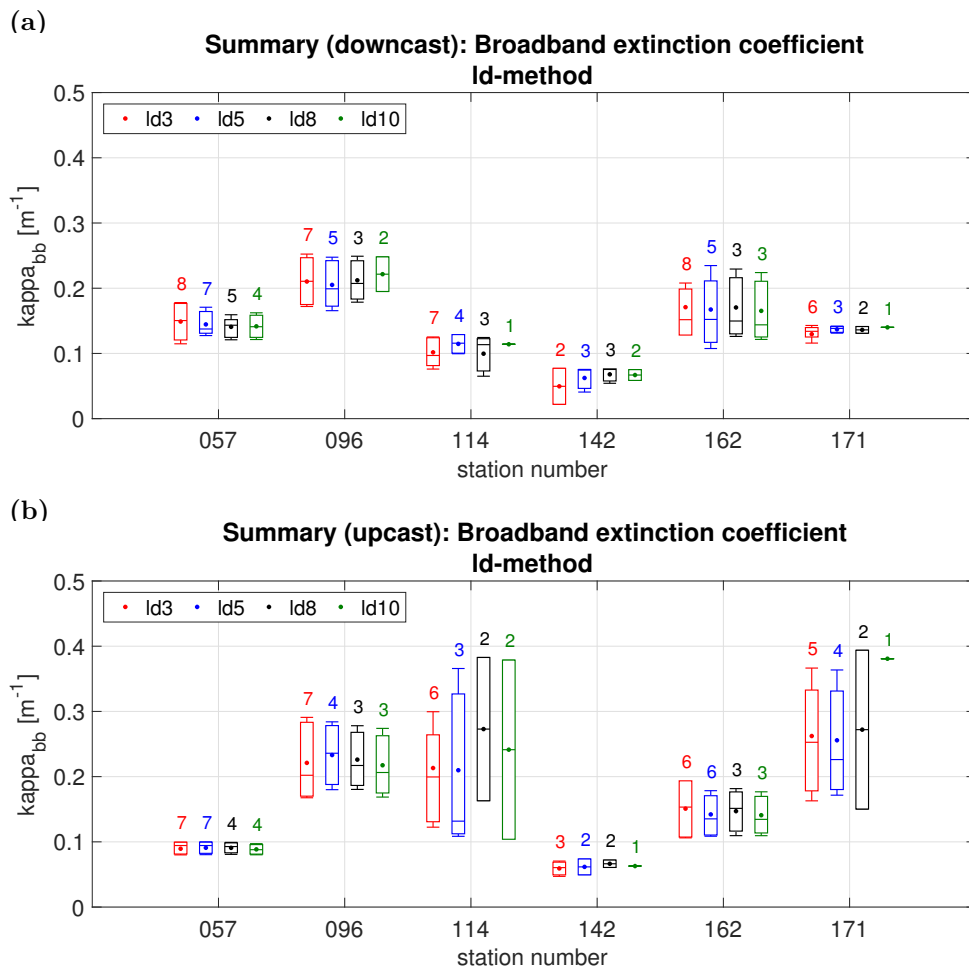

Figure 5.1: Box plots for the broadband extinction coefficients computed for the (a) downcast and (b) upcast results for all ice stations during PS101. The values shown are obtained using the *ld*-method. The *ld*3-scenario is given in *red*, *ld*5 in *blue*, *ld*8 in *black* and *ld*10 in *green*. Boxes are the first and third quartiles, whiskers show the 20th-and 80th-percentile of the broadband extinction coefficients of the respective scenario. Dots indicate the mean, dashes the median values of the broadband extinction coefficients. The number next to the boxes gives the number of coefficients available from the respective scenario fit for the statistic.

The two case studies support the assumption that broadband extinction coefficient estimates are subject to a number of influences, such as general ice and water conditions, that vary from station to station. Furthermore, different operators have different ROV piloting routines, which introduces variations in the depth profiles. Finally, the results are influenced by subjective profile data selection during processing and the different methods applied for the fitting. Considering these factors at all stations, it is not possible to compare methods and scenarios on the basis of individual profiles.

5.1.2 Cast, method and scenario comparison

Estimated broadband extinction coefficients of the two cases indicate that the water properties vary significantly between stations. Measurements are locally influenced by the specific properties and characteristics at that station. This is particularly evident in the broadband extinction coefficient data (Figure 5.1, Table 4.1). Hence, for the purpose of identifying the superior method and the appropriate scenario for future analyses of layers with different optical properties along ROV depth profiles, single profiles are not sufficient. Instead of analysing the six stations individually to compare approaches and scenarios, the following section combines the RAMSES broadband extinction coefficient estimates and the corresponding R^2-values of all stations for the comparison.

Up- versus downcast

The PS101 ROV piloting team pointed out that the upcast transmittance data is likely less useful for the analysis, as the upcasts were executed less cautiously. Generally, this is confirmed when comparing the up-and downcast broadband extinction coefficient estimates of all stations (Figure 5.1). Figure 5.1 shows broadband extinction coefficient box plots for the different scenarios at the different stations. Stations 096, 114 and 171 stand out as cases where estimates from the two casts are not only different in spread for the four scenarios but also in actual mean and median values. Spreads between the first and third quartiles of the four scenarios at the downcast of station PS101-114 range between approximately 0.07-0.12 m^{-1}. The same inter-quartile spread ranges from approximately 0.12-0.38 m^{-1} for the upcast of the same station. These differences between up-and downcast results can have two explanations. First, up-and downcast were sampled inconsistently. Second, the two casts sampled two completely different water columns with significantly different broadband extinction coefficients along the depth profiles. The latter explanation is unlikely due to the measurement setup of the depth profiles. Furthermore, the broadband extinction coefficients from stations 057, 142 and 162 show more similar scenario spreads for the up-and the downcast. Hence, it is assumed that the upcast transmittance data is indeed less useful, and so the following method and scenario comparison is limited to downcast data only.

Number of data points nm versus layer thickness ld

Based on broadband extinction coefficients from the downcasts of the different stations (Figure 5.2), ld-and nm-method results are very similar. Differences are more evident in
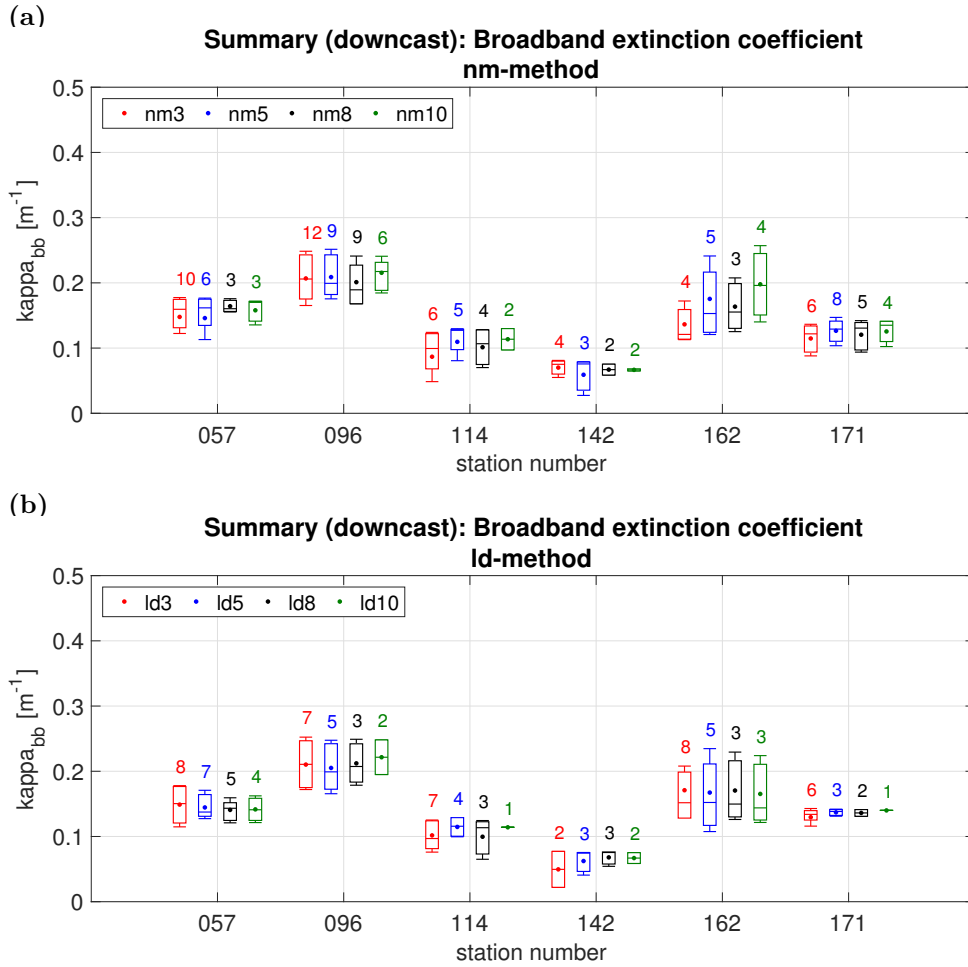
(a)

(b)

Figure 5.2: Box plots for the broadband extinction coefficients computed for the downcast calculations for the (a) *nm*-method (*nm*3 in *red*, *nm*5 in *blue*, *nm*8 in *black* and *nm*10 in *green*) and (b) the *ld*-method (*ld*3 in *red*, *ld*5 in *blue*, *ld*8 in *black* and *ld*10 in *green*) for all ice stations during PS101. Boxes are the first and third quartiles, whiskers show the 20th-and 80th-percentile of the broadband extinction coefficients of the respective scenario. Dots indicate the mean, dashes the median values of the broadband extinction coefficients. The number n above the boxes gives the number of coefficients available from the respective scenario fit.

the extinction coefficient spreads (*ld*3 versus *nm*3, *ld*5 versus *nm*5, *ld*8 versus *nm*8 and *ld*10 versus *nm*10) of individual scenarios. These variations most likely occur because each method fits an exponential function to a different number of data points. This results in varying numbers of fits (n) available for statistical analysis. Utilizing more data points for individual fits results in a fewer number of fits along the profile. The quality of the fit might increase, but the resolution of the water column decreases. Small variations in the scenario results are merely introduced by the different approaches applied for the fitting. However, similar broadband extinction coefficient results for the scenarios of the two methods do not necessarily prove that the two methods perform equally well. Hence,

the R^2-value is analysed as it gives the ratio between variability explained by the fit and actual data variability.

Figure 5.3 displays the corresponding R^2 box plots for the broadband extinction coefficient values of each station downcast. Additionally, the figure shows box plots of the summary of R^2-values from all stations (*right* part of the figure). R^2-values for the four scenarios of the individual stations confirm that each station is unique and distinct layers should be investigated separately for each station. Fits at station PS101-057, for example, explain a relatively high percentage of the transmittance data variability with mean and median R^2-values larger than 0.7 for all scenarios of the two methods. The largest R^2-value spreads between first-and third quartiles are about 0.3 (*ld*3, PS101-057), which is fairly small compared to other stations. The least agreement between R^2-values of individual scenarios is apparent at station 162. The R^2-spread ranges from approximately 0.4 (*ld*8) to about 0.7 (*ld*3).

In contrast, comparing the summary of all R^2-values for the scenarios and their methods
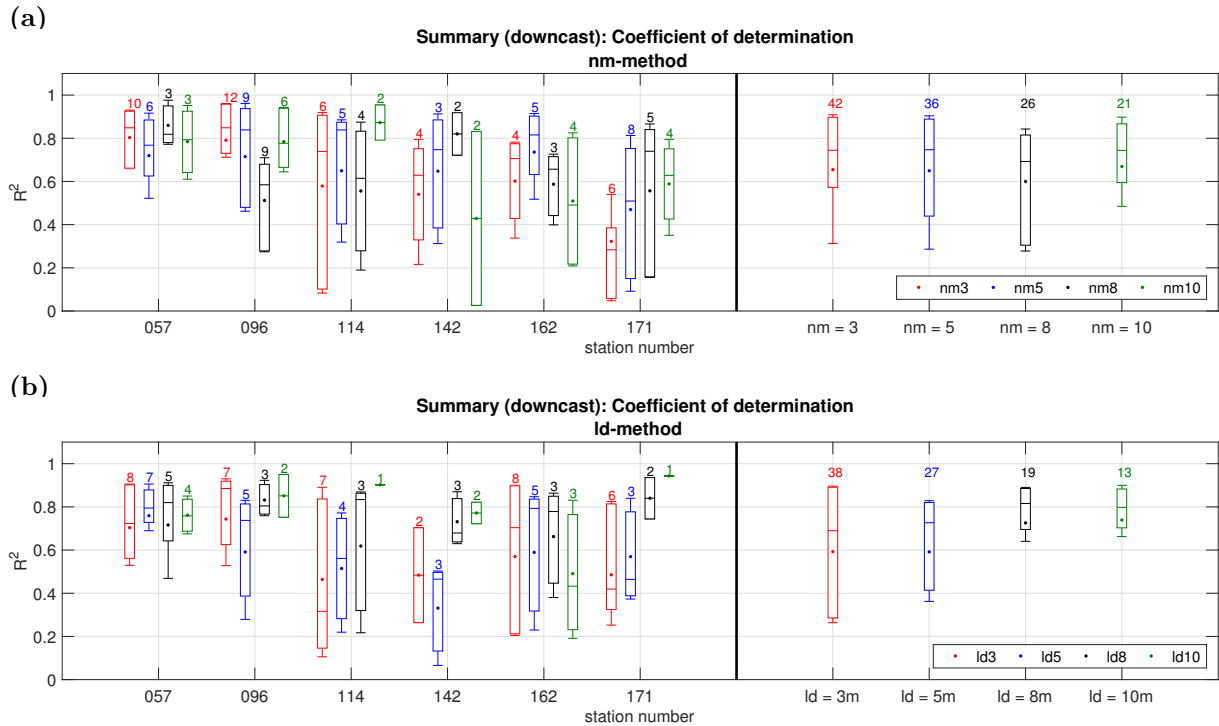
(a)

(b)

Figure 5.3: Box plots for the R^2-values corresponding to the broadband extinction coefficients (Figure 5.2) of the different scenarios at PS101 ice stations. The *left* part displays (a): the downcast results for the *nm*-method (*nm*3 in *red*, *nm*5 in *blue*, *nm*8 in *black* and *nm*10 in *green*). *ld*-method (*ld*3 in *red*, *ld*5 in *blue*, *ld*8 in *black* and *ld*10 in *green*) values are shown in *left* part of (b). Boxes are the first and third quartiles, whiskers show the 20th-and 80th-percentile of the R^2-values of the respective scenario. Dots indicate the mean, dashes the median values of the R^2-values. The number n above the boxes gives the number of coefficients available from the respective scenario fit. The *right* parts show box plots of the summary of R^2-values from all stations together (same color code as for the *left* of the figure.)

42

provides an idea of how well the methods perform. Both methods show a smaller spread in the respective scenarios that utilize more data points for the fitting process ($ld8$, $ld10$, $nm8$ and $nm10$). This is more pronounced for the ld-method. One of the most important parameters, when comparing the two methods, is the number of R^2-values available for the respective scenario fit statistic (n, shown above the respective box). Due to the different data point selection for the fitting process, the nm-scenarios have more R^2-values available than their ld-method counterparts (for example, $nm3$-scenario: $n = 42$ versus $n = 36$ for the $ld3$-scenario). Again, this indicates higher resolution is obtained by the use of the nm-method, but possibly more reliable fits are obtained using the ld-method. This is confirmed by the fact that every ld-scenario summary, except $ld3$, shows a smaller R^2-spread than the associated nm-scenario summary. In addition, mean and median R^2-values for the scenarios $ld3$ and $ld5$ are lower than for the corresponding nm-scenarios, while they exceed their counter-values for the scenarios $ld8$ and $ld10$.

All in all, the ld-method seems superior to the nm-method for the 8-and 10-scenarios, while 3-and 5-scenarios are fairly similar. This is valid for the specific downcast data sets of PS101. However, the disadvantage of the ld-method is the unknown number of data points used for the individual fits. Some fits might be calculated with only two data points, while others are based on a much higher number of points. Therefore, the consistency in measurement frequency along the depth profiles is crucial for future studies. Despite the knowledge of the exact number of data points utilized for the nm-fits, varying measurement frequencies lead to large data gaps along the profile. The same number of data points used for nm-fitting can cover fundamentally different depth ranges, making smaller differences in the water column more difficult to discern. In contrast to the ld-method, the nm-method provides no information about the depth range, which is a clear disadvantage when investigating distinct layers in the water column.

Based on this analysis, a more cautious handling of the ROV during depth profiles is required in order to improve broadband transmittance data sets. Sampling the water column more regularly further improves the ld-method and is of great importance to take full advantage of this method.

Scenarios

As the ld-method is identified as the superior method for the given data set, the next step is to determine the best scenario for the analysis. As mentioned before, two assumptions influence the scenario decision. First, the number of data points available influences the ratio of variability that is explained by the fit. On the other hand, the goal is to provide a resolution as high as possible in order to find differences in the properties of water layers. Without any additional information on the depth profile, the ld-value is selected to be small in order to resolve property changes on small vertical scales along the profile. However, as evident from the R^2 summary plots (Figure 5.3b), smaller scenario numbers coincide with more variation in the R^2-values. The fits explain the actual data variability to strongly varying degrees. This occurs as the broadband transmittance profile changes with depth. While values from the entire cast indicate an exponential decay in broadband transmittance, individual parts can show different relationships. The decay in broadband transmittance in the water column is still exponential, but this is not evident in theses

small selections of data points. This apparent change in decay predominantly occurs in the deeper layers of the profile where broadband transmittance tends towards zero and noise signals dominate. Fitting a layer with a small number of data points may not be possible with the selected model, as small numbers of data points do not display the prevailing exponential decay correctly. Assuming that a larger number of data points increases the chance of a fit that better explains data variability, scenarios $ld8$ and $ld10$ are preferable over the other scenarios. As the box plots indicate, the R^2-value spread is smaller for these scenarios than for the other scenarios (Figure 5.3b). Simultaneously, when the thickness of the water layer (ld) is increased, the number of fits along the profile is reduced (smaller n for the scenario box plots at the individual stations). Fewer layers are resolved.

All in all, there is strong evidence that the scenarios $ld8$ and $ld10$ show the highest and most consistent R^2-values. The increase in scenario number is accompanied by seemingly better fits. However, as the broadband transmittance profile changes with depth, applying a combination of scenarios might be a compromise between higher resolution and higher quality fits.

5.1.3 RAMSES versus VIPER

In order to validate the RAMSES broadband extinction coefficient estimates a hyperspectral extinction sensor (VIPER) measured absorbance spectra parallel to the RAMSES measurements. These values are calculated into broadband extinction coefficients integrated over the PAR-range to compare them to PAR extinction coefficients estimated from the RAMSES transmittance data.

The comparison between VIPER and RAMSES PAR extinction coefficients shows two major challenges. First, the limited number of VIPER measurements are unevenly distributed along the casts of the two stations (PS101-114 and 142). This leads to difficulties in comparing VIPER data from up-and downcast of individual stations. Secondly, RAMSES results suggest that the PAR extinction coefficients along the downcasts of both stations are below the detection minimum of the VIPER (0.1535 m^{-1}).

The variability of the VIPER PAR extinction coefficient values at station PS101-114 is explained by the beam attenuation coefficient spectra presented in Chapter 4.2 (Figure 4.10). Apart from values between 400 and 450 nm, spectral beam attenuation coefficients are dominated by noise and below the detection minimum of the VIPER at all depths. Accordingly, integrating over the PAR range yields PAR values that are dominated by noise as well. Therefore, the PAR extinction coefficients calculated from the VIPER data are not reliable at that station and no rational comparison is possible.

The analysis of the VIPER beam attenuation coefficient spectra at station PS101-142 shows that, although confined wavelength ranges are dominated by noise (between 470 to 500 nm and between approx. 600 to 700 nm), all values are within the detection range (Figure 4.11). Assuming that the VIPER PAR extinction coefficients at that station are useful, the values are compared to PAR extinction coefficient values estimated from RAMSES data (Figure A.3). As discovered above, extinction coefficients estimated from the downcast RAMSES data using the ld-method are superior to values obtained during
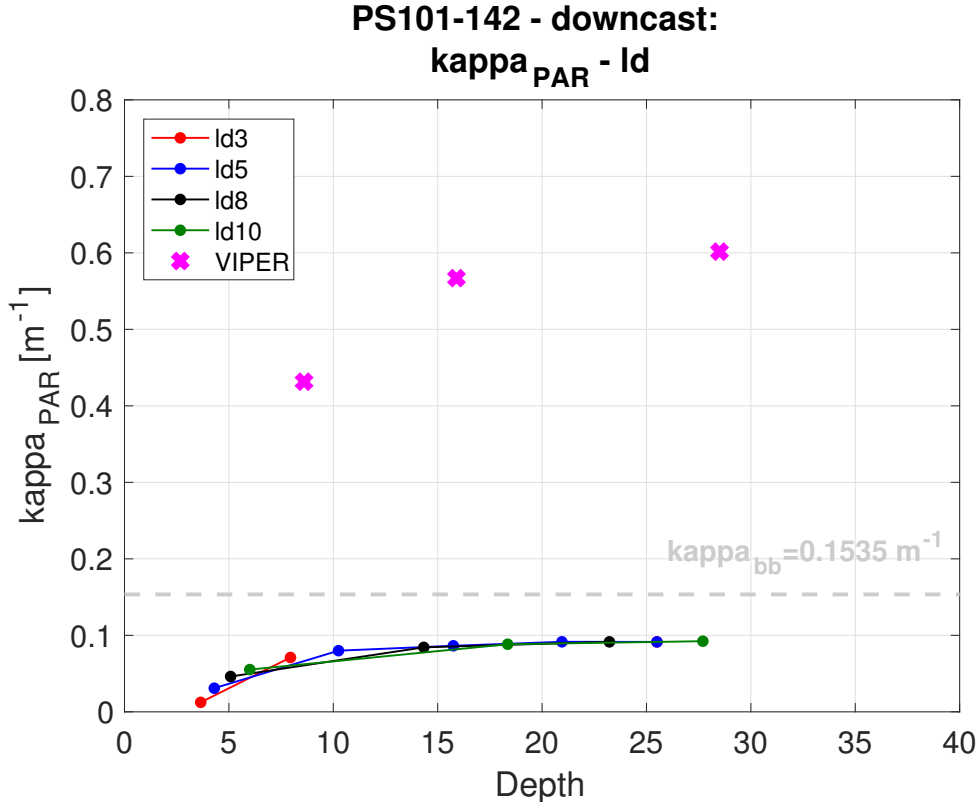
Figure 5.4: PAR extinction coefficients calculated from the RAMSES and VIPER (x-markers) data for the downcast of station PS101-142. RAMSES PAR extinction coefficients are estimated using the *ld*-method. *Red* dots indicate the *ld*3 scenario, *blue* shows *ld*5, *black ld*8 and *green ld*10 results. The dotted *grey* line indicates the minimum broadband extinction coefficient detectable with the current VIPER setup (optical path length: $0.15\,\mathrm{m}$).

the upcast and using the *nm*-method. Therefore, Figure 5.4 shows the presumably best available PAR extinction coefficient estimates available from the two sensors at station PS101-142. The available VIPER values range from approximately $0.42\,m^{-1}$ at $8\,\mathrm{m}$ to roughly $0.6\,m^{-1}$ at $29\,\mathrm{m}$ depth. These values are about 5 to 6 times larger than the corresponding RAMSES estimates. These deviations may occur due to the fundamentally different measurement setup of the two sensors. The VIPER measures a single beam emitted from one light source. The light beam loses intensity through absorption and scattering. In contrast, the RAMSES collector plate measures the diffuse light field of the half space above the sensor. Accordingly, VIPER beam attenuation coefficients are expected to be larger than the extinction coefficients estimated using the RAMSES transmittance data. The impact these differing setups have on the differences between the results from the two sensors is not quantified. However, considering the clarity of the Arctic Ocean the differences evident in Figure 5.4 seem to be too large to be only caused by differing measurement setups.

Nevertheless, it is clear that the number of measurements is too small to have a meaningful discussion about the performance of the two sensors. Only a few VIPER measurements

exist along the profiles of two stations. The ones that are available are unevenly distributed along the casts, which makes it unfeasible to compare up-and downcast results. Additionally, a rational comparison to PAR extinction coefficients estimated from RAMSES data is not possible. Even if the VIPER coefficients are reliable, the sensor's coverage of the profile is not sufficient. The values available could be outliers, and with the lack of additional data, a validation of the presented results is not possible.

5.2 Spectral beam attenuation coefficient

The spectral beam attenuation coefficients available from the two VIPER stations support the analysis of the PAR extinction coefficient results from the VIPER. It is evident that the spectra at station PS101-114 are dominated by noise. Nevertheless, spectral beam attenuation coefficients from stations PS101-114 and PS101-142 indicate an increase with depth within the PAR-range. Although the spectral patterns are similar between 400 and 460 nm, beam attenuation coefficients are significantly different between the two stations. The absolute maxima at each station occur at approx. 412 nm. The beam attenuation coefficient at 412 nm during the downcast of station 114 is approximately $0.5\,m^{-1}$ at 33.3 m depth, while the downcast maximum at station 142 is approximately $0.95\,m^{-1}$ at 28.5 m depth. As spectra from station 114 are close to, or below the detection minimum of the VIPER throughout the entire PAR-range, this discussion focuses on results from station PS101-142.

As the VIPER measurements took place at different depths during up-and downcast, comparing the casts is challenging. Downcast spectral beam attenuation coefficients at 8.6 m (15.9 m) and upcast values at 9.4 m (14.5 m) are rather different. At approx. 9 m, the spectral maximum at 412 nm reaches $0.83\,m^{-1}$ for the downcast and close to $0.95\,m^{-1}$ for the upcast. At about 15 m depth the difference at 412 nm is even more substantial. Values reach approximately $0.83\,m^{-1}$ (downcast) and $1.1\,m^{-1}$ (upcast). These differences are similar along all wavelength ranges that are not dominated by noise.

One possible explanation for these deviations is the mixing of the water column by the ROV. The VIPER is located at the bottom of the ROV. Therefore, downcast measurements are taken in unaltered water, while upcast measurements are taken in a medium that has been mixed by the ROV's vertical motion and the rotation of the thrusters. Following these alterations of the water column up-and downcast measurements at similar depths are expected to be rather different. With the apparent increase in spectral attenuation with increasing depth (Figure 4.11) it is evident that upcast spectral beam attenuation coefficients are larger than their downcast counterparts at similar depth. With mixing as the dominant factor controlling the differences between up-and downcast results, this is expected. However, the differences evident in the data (Figure 4.11) are of the order of roughly 14% at 9 m and approximately 25% at about 15 m depth. These values are comparably high, which suggests additional influences. Unfortunately, due to the fact that only measurements from station PS101-142 provide useful data, a validation of those results is not possible. Furthermore, the lack of spectra along the depth profile is an additional factor obstructing this analysis. With the given data set, a meaningful

discussion about the changes in beam attenuation coefficient spectra along depth profiles in the Arctic Ocean is not possible.

VIPER measurements need to be taken more often than it has been the case during PS101. Due to the comparably low measurement frequency of between 1 and 3.5 min, the time used to record a depth profile needs to be increased. Currently only about 5 measurements are taken during a descent of approximately 50 m. Considering the possibility of erroneous recordings, there is no sufficient amount of measurements for meaningful analyses of the water column. Furthermore, with the current variations in the measurement frequencies certain depths are sampled multiple times while other depth ranges are not represented at all. Therefore, the cast focusing on the recording of absorbance spectra with the VIPER is required to last significantly longer. Slower descents during VIPER casts would not only provide more data points along the profile, but also cover all depths of the sampled water column.

5.3 Supporting bio-optical data

Until now, the identification of water layers with distinct optical properties was attempted using RAMSES transmittance and VIPER absorbance data. The first approach implemented different fitting methods to estimate broadband extinction coefficients. The second method utilized a small number of direct measurements which were unevenly distributed along the depth profiles. Current VIPER measurements are insufficient for the desired analysis. In contrast, the number of RAMSES transmittance measurements along the depth profiles is adequate. However, the analysis showed that the methods selected for the investigation of distinct layers using the RAMSES data, are still premature and require improvements of the measurement and data processing techniques. Results from individual stations indicated changes in broadband extinction coefficients along the depth profiles, but the identification of distinct layers is not yet possible. More importantly, the direct determination of the boundaries between adjacent layers is not achievable.
Following the analysis, it is evident that additional information is required for the desired investigation. While, PS101 temperature, salinity and pH measurements from the ROV are unreliable, backscatter, FDOM, and chlorophyll concentration data from the ECO-Triplet provide additional information essential to this work's analysis.
Figure 5.5 shows downcast values of chlorophyll concentration, backscatter and FDOM for all PS101 ice stations. A decrease in backscatter and chlorophyll concentration from the first (057) to the last (171) station is evident. Stations 057, 096 and 114 show comparably high chlorophyll concentrations (approximately 0.7, 0.5 and $0.4\,\mu g/l$, respectively) and backscatter values (approx. 2.2×10^{-4}, 1.5×10^{-4} and 1.4×10^{-4}, respectively) in the upper part of the cast. At depths between 20-30 m, values for both parameters drop noticeably to match the values measured at stations 142, 162 and 171. These results reveal water property changes associated to the change in season. While measurements at station PS101- 057 were taken right after the sea- ice minimum (September 13, 2016) on September 15, 2016, PS101-171 measurements were conducted later in the freeze-up season, on October 1, 2016. The FDOM data indicates very similar values for stations 096
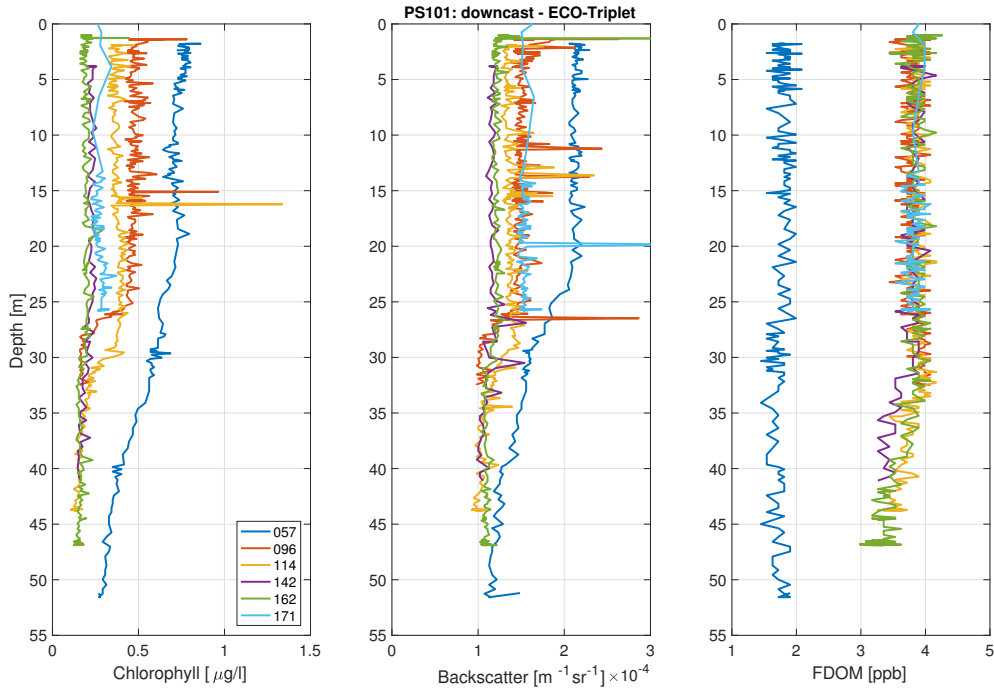
Figure 5.5: Values of chlorophyll concentration ($[\mu g/l]$, *left*), backscatter ($[m^{-1}sr^{-1}]$, *middle*) and FDOM ($[ppb]$, *right*) retrieved from the ECO-Triplet sensor. Measurements are taken during the downcasts of the six stations of PS101.

to 171 (between 3.5 to $4\,ppb$), while FDOM was noticeably lower at station 057 (between 1.5 and $2\,ppb$).

Chlorophyll concentration and backscatter values indicate pronounced biological activity at the first three stations that reduced towards the end of the campaign. Within the first three stations, different chlorophyll concentrations and backscatter signals are apparent along the downcasts. The tendency of biological activity reducing throughout the sampling period of PS101 is also apparent in the downcast RAMSES broadband extinction coefficients estimated for each of the six stations (Table 4.1). Broadband extinction coefficients decrease from station 096 ($0.2378\,m^{-1}$) to station 142 ($0.0694\,m^{-1}$).

Higher chlorophyll concentrations are associated with more extinction in the water column. However, the water column at station 057 shows the highest chlorophyll concentrations of all stations, nevertheless, the broadband extinction coefficient ($0.1396\,m^{-1}$) is smaller than for station 096. This is most likely caused by the low FDOM values in the water column of station 057. These results indicate that the optical properties of seawater are controlled by multiple biological parameters that have very different impacts on the extinction within the medium. The decrease in extinction coefficients with a decrease in biological matter confirms findings of Taskjelle et al. (2016). They found that increased biological activity has the potential to increase absorption in the upper $20\,m$ of the water column noticeably.

Figure 5.6 a shows downcast chlorophyll concentration and backscatter values obtained at station PS101-114. Chlorophyll concentration remains at approximately $0.37\,\mu g/l$ throughout the upper 30 m of the cast. A distinct drop to roughly $0.16\,\mu g/l$ is apparent between 30 and 32 m depth. The layer extending below this depth shows chlorophyll concentrations of $0.15\,\mu g/l$ down to end of the profile. The same distinct boundary is evident in the backscatter data. Backscatter values are centred around $1.3 \times 10^{-4} m^{-1} sr^{-1}$ throughout the upper 30 m and drop to roughly $1 \times 10^{-4} m^{-1} sr^{-1}$ below. Both data sets suggest a layer with higher particle concentrations located above a layer that is less contaminated. These layers only occur at the first couple of stations and are caused by the accumulation of biological matter under the ice cover during the melt season. This activity is favoured by the fact that the ice is more light-permeable during the summer months. During the freeze-up less light reaches the under-ice water layer, and biological activity reduces.

The presented ancillary information is used to specifically select data points from optically different layers for the fitting of the RAMSES broadband transmittance data. Figure 5.6 b shows the exponential fits plotted onto the broadband transmittance. The upper (lower) layer estimate shows a κ_{bb}-value of $0.1142\,m^{-1}$ ($0.0636\,m^{-1}$). While $R^2 = 0.9513$ for the upper fit, $R^2 = 0.2261$ for the fit below 30 m. These changes in the optical properties of individual layers are strongly linked to the amount of biological matter in the water
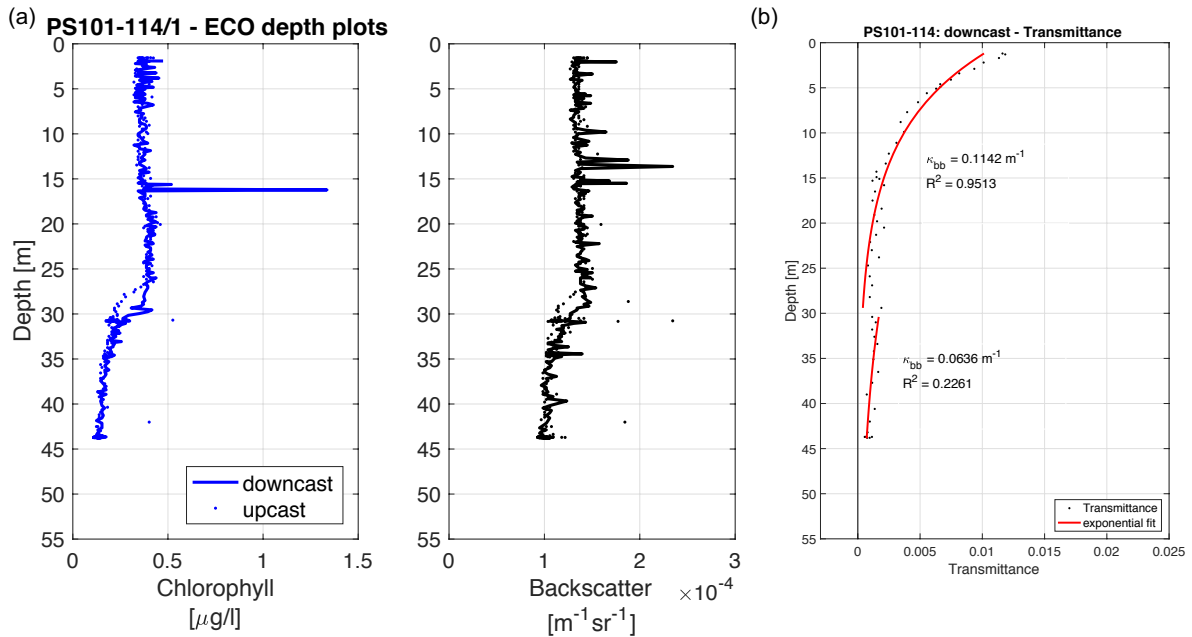

Figure 5.6: Values of (a) chlorophyll concentration ($[\mu g/l]$, *left*) and backscatter ($[m^{-1} sr^{-1}]$, *right*) retrieved from the ECO-Triplet sensor. (b) exponential fits (*red* lines) projected on RAMSES broadband transmittance data (*black* dots). κ_{bb}-values indicate the estimated broadband extinction coefficients of the respective layer. R^2-values represent the fraction of total broadband transmittance variability that is explained by the fit. All measurements are taken during the downcast of station PS101-114.

column, however, the given data set is insufficient to provide a quantitative description of this relationship.

The presented results indicate that the identification of distinct layers is possible using the given RAMSES data. Estimating broadband extinction coefficients from broadband transmittance data with the selected exponential decay model is achievable, but without extra data from other instruments the presented methods are too limited to find the boundaries between layers with distinct optical properties. The presented exponential fitting methods are limited in parts of the profile where broadband transmittance values approach zero. Moreover, the quality of the RAMSES transmittance data limits the quality of broadband extinction coefficient estimates and the availability of VIPER measurements is not sufficient.

5.4 Uncertainties and error sources

The following section provides a detailed description of possible error sources during data retrieval with the presented sensors. Furthermore, the influences of the different analysis methods on the results are discussed.

5.4.1 Sensors

No instrument is entirely accurate. Measurement uncertainties of the sensors used for this analysis are presented in Chapter 3. Beside the general uncertainties, RAMSES transmittance values are influenced by the fact that inter-comparison between the on-ice and below-ice RAMSES sensors was not possible for this study. Although the TriOS sensor calibration is considered sufficient for the purposes of this study, an error is introduced. The necessary interpolation of the data, as well as the data processing done prior to the analysis, facilitate the propagation of errors.

On the other hand, VIPER absorbance spectra are promising as they measure inherent optical properties of the water that are independent of a fitting method and the incoming light field. Even so, the presented VIPER measurements are too sparse and strongly limited by the detection minimum of the sensor. The dominant noise signal visible in the beam attenuation coefficient spectra strongly alters the calculated PAR-integrated extinction coefficients. In addition to measurement uncertainties and errors introduced during processing, the entire VIPER setup limits this analysis. VIPER measurements conducted in comparable studies have generally focused on highly contaminated waters from surf zones and estuaries. The study by Ramirez-Perez et al. (2014) investigated different shapes of beam attenuation coefficient spectra in order to retrieve information about particle size and concentration. While the VIPER is useful for the analysis of those highly polluted waters, the current setup is impractical for the clear water of the Arctic Ocean.

5.4.2 Exponential fitting

For the purpose of identifying water layers with different optical properties, an exponential decay model (Equation 3.2) is used to estimated broadband extinction coefficients from RAMSES broadband transmittance values along depth profiles. This specific model is chosen due to its simplicity compared to other models (Frey et al., 2011). The snow and ice conditions apparent during PS101 were less complex than in the Frey et al. (2011) case, and the model is considered sufficient for the purpose of this study. Nevertheless, the under-ice light field is not only impacted by varying ice-surface characteristics, like melt ponds and snow-free ice, but also differing ice types and ice thicknesses. The entire RAMSES transmittance data analysis is solely based on incoming solar irradiance. Thus, the integral over the downwelling radiance not only consists of direct light from above but also from light scattered by other features. As Katlein et al. (2016) showed, irradiance sensors do not account for horizontal and vertical light field variations associated with sea-ice inhomogeneity. Accordingly, the transmittance data utilized in this study is influenced by the prevailing ice types, surface conditions and sea-ice topography. Despite the mentioned influences, the exponential decay model is still used as geometric effects on the light field are less pronounced in the given data set. Additionally, scattering from water particles is limited in the clear Arctic Ocean (Katlein et al., 2016). Lastly, the vertical effects associated with ridges and melt ponds (Katlein et al., 2016) are not visible in the given data set. Broadband transmittance shows an exponential decay from the ice-ocean interface towards depth.

All in all, the heterogeneity of the sea-ice cover and the associated effects on the spatial light distribution are a factor influencing the measurements. However, given the general ice conditions during PS101 ice stations, the presented model is still considered useful for the presented analysis.

In order to determine changes along the profiles, two multiple fitting approaches are developed. Estimated broadband extinction coefficients are strongly impacted by the data points used for the fitting process. The presented nm-method utilizes a predefined number of data points for the individual fits. In contrast, the ld-method uses all data points within a layer of pre-defined thickness. The quality of each fit is dependent on the number of data points available for the calculation. A major error source for the fitting of the data is multi-sampling. Multiple data points measured at similar depth can influence the fitting result significantly. Therefore, the higher the number of data points used for the fit, the smaller the impact of multi-sampling.

An additional factor is the broadband transmittance profile itself. The given PS101 profiles all indicate exponential decay with depth. However, data points from individual parts of the profiles do not show the expected exponential decay. The general decay remains exponential but due to strong data variability and noise the presented model is not functional for the data points in these parts. This is the case especially in the lower parts of the depth profiles, where broadband transmittance values tend towards zero, and for small numbers of data points that are used for the fit (e.g. $nm3$ and $ld3$). Consequences are either no fits in these parts or small R^2-values for the estimated broadband extinction coefficients.

A major part of this study focused on the method and scenario comparison to overcome these error sources. However, a combination of different scenarios and methods may improve the broadband extinction coefficient estimates along a depth profile in future studies. Applying additional exponential decay models that account for more complex ice-surface conditions could improve the results as well.

The analysis indicates that the method utilizing all data points within a layer of predefined thickness (*ld*-method) is advantageous over the method using a pre-defined number of consecutive data points for the fitting process. More precisely, the *ld*-method is considered superior for layer thicknesses (*ld*) of 8 and 10 m. However, the analysis also discovered that this might only be the case for the given PS101 broadband transmittance data set. Future fitting approaches could fit broadband transmittance data from sliding sections rather than fit predefined sections of the profile. Fitting sliding sections may also enable future studies to identify boundaries between optically differing layers on the basis of RAMSES broadband transmittance data only.

Every individual data set is different and no general fitting solution is applicable for every station. Furthermore, this study finds that the selected exponential decay model is not applicable for the entire broadband transmittance depth profile. The data quality changes along the profile and when examining small sections of it other models possibly increase the percentage of variability that is explained by the fits. Applying a different model could also support the increase in resolution at depths that show a differing relation between broadband transmittance and depth. More importantly, data quality and signal to noise ratio have to be increased to display the expected exponential decay at all depth ranges.

5.4.3 ROV depth profile routines

The general operating routines of the ROV are of great importance. Differences at individual stations occur naturally. Unfortunately, the results presented show that differences between station and casts also occurred due to differences in conducting the profiles. Differences in vertical ROV velocities introduced varying measurement frequencies along the profiles. Subsequently, the fitting of the transmittance data was influenced. A consistent time plan for the different casts of the profile is required in order to make stations comparable. Depending on the availability of light at depth, individual profiles always cover varying depth ranges. However, maintaining the same speed over same vertical distances would improve the comparability of the stations. This is valid even if the profiles are different in length. Consistent vertical sampling may also overcome the strong broadband transmittance variability evident in the deeper layers. Less variability would improve the fitting process and possibly yield more reliable estimates for broadband extinction coefficients.

More consistent planning of the profiles is not just required for the RAMSES sensor but also for the VIPER. In order for the VIPER to measure properly, water flows into the device and is sampled. The integration time of this sampling process can be up to 20 s. Following that the ROV would have to remain at that same depth for the entire integration time of the instrument. Total dive times of the casts at the two VIPER stations were roughly 5 min (3 min) at station PS101-114 (PS101-142). Accordingly, instead of

sampling water at one depth, the ROV movement led to measuring water from multiple depths. As the integration time was much slower than 20 s during PS101, this influence is rather small but still provides an error source. Again, adjusting the ROV speed along the profile would significantly improve the obtained data set.

However, ROV profiles are not just influenced by the operator's steering skills. Errors are also introduced through outside influences like currents. Preventing lateral movements of the ROV during depth profiles is extremely challenging. Especially currents can tilt the ROV, which alters the field of view of the RAMSES sensor and ultimately the obtained data. Additionally, the movement of the ROV through the water column is an alteration of the observed system. Vertical movement and thruster rotation are sources of mixing. When determining small scale changes in the water layers along a depth profile, this mixing has the potential to obfuscate the true signal. However, these are influences introduced by the selected method of sampling the water column and therefore must be accepted prior to the measurements.

All in all, numerous ROV-related error sources potentially alter the measurements. Some are general influences that are introduced through the method of measuring with robotic vehicles. They are accepted, as the only possibility to prevent them is to select a different measurement setup. The advantages of the small logistical footprint, the comparably easy handling and the reach of the ROV system are considered to clearly outweigh the measurement uncertainties introduced by the method. However, the presented analysis also indicates that errors are induced due to the current execution of the depth profile measurements. These errors can be overcome by careful planning of the individual casts and cautious handling of the ROV.

5.4.4 Data limitations

Finally, the limitations in VIPER measurements prohibit a meaningful analysis of the water column. VIPER measurements are too sparse to validate RAMSES measurements. Furthermore, due to the inconsistency of the profiles, the developed fitting methods for the RAMSES transmittance data are not able to estimate extinction coefficients to their full potential. However, even after improving the ROV operations and obtaining more consistent measurements from the VIPER, data from the other ROV instruments is required to complement the findings of optically different layers along the depth profiles. The ability to detect boundaries between individual water layers is especially dependent on measurements of additional water properties.

Optical properties of the under-ice water layers are especially important for the investigation of the changing energy budget at the ice-ocean interface. Unfortunately, ROV temperature, salinity and density data is not available from the PS101 campaign. These additional data sets could complement future analyses and support detailed calculations of heating rates in the upper ocean layers. These additional investigations would enhance the knowledge about the impact of the increasing amount of light that penetrates the under-ice ocean.

6. Summary and conclusions

Current changes in the Earth's climate strongly impact the Arctic sea-ice cover. The decrease in sea-ice extent and thickness mark a strong interference in the Arctic environment. The insulating boundary between ocean and atmosphere is reduced, which leads to substantial changes in the Arctic energy budget. The decreasing sea-ice cover favours the transmission of solar shortwave radiation into the ocean. The associated increasing energy input has strong implications for the upper ocean environment. In order to determine the impact of water properties on the available light field in the upper ocean, this study utilizes optical data retrieved by a remotely operated vehicle (ROV) during the 2016 *RV Polarstern* campaign PS101. The focus of this analysis is on the vertical changes along depth profiles during the ice stations of the expedition.

6.1 Key findings

Broadband transmittance data fitting
Two different multi-fitting approaches are investigated in order to determine the superior method for the estimation of broadband extinction coefficients from broadband transmittance data using an exponential decay model. The ability to explain the total broadband transmittance variability along the profile and the resolution of the water column are the two parameters that are most important for selecting the superior method. The analysis reveals that the *ld*-method with layer thicknesses of 8 or 10 m (*ld*8, *ld*10) is the prime fitting method for the given data set. However, the reliability of the exponential decay model reduces along the depth profile. In addition, it is evident that the individual stations have to be investigated separately. Overall, it is concluded that the presented methods are applicable to broadband transmittance data of depth profiles. However, in order to improve future analysis using RAMSES broadband transmittance data:

- a combination of fitting methods and models is required for the investigation of optical property changes along a depth profile

VIPER extinction sensor
The VIPER extinction sensor measurements conducted during PS101 are unusable for investigating oceanic optical properties under sea ice. Two major limitations are discovered:

- measurements along the profiles of PS101 are too sparse

- the instrument setup is impractical for the clear water conditions below Arctic sea ice in autumn

Supporting data
The estimation of broadband extinction coefficients along a depth profile is possible using RAMSES broadband transmittance data. However, the recognition of boundaries

between optically different layers cannot be achieved without the support of additional data sets. The ECO-Triplet backscatter and chlorophyll concentration depth profile data are considered supplements to the presented RAMSES data. Backscatter and chlorophyll concentration data along the depth profiles reveal the following results:

- distinct layers occurred due to presence of biological matter in the water layers at stations 057, 096 and 114

- stations 142, 162 and 171 do not show the same layering

The transition from the melting season towards the freeze-up season is assumed to be responsible for the dissipation of these layers in the later profiles. As less light is available, biological activity is reduced. Chlorophyll concentration, backscatter and FDOM data also provide insight into the causes of differences in the extinction coefficients. Currently, other sensors like the GPCTD or the pH-sensor do not provide useful data to validate and complement the presented results.

6.2 Future operation of the ROV system

When considering the depth profiles from the ice stations individually, it becomes evident that improvements of the ROV operating routines are crucial for future investigations. The most important modification necessary is:

- the adjustment of the depth profile sampling to the instruments

Different instruments require different profiles. The quality of the extinction coefficient estimates from RAMSES broadband transmittance data is dependent on the consistency in the measurement frequency. The vertical velocity needs to be constant throughout the profile, as pauses along the cast lead to multi-sampling and complicate the fitting process. In contrast, VIPER profiles need to be conducted much more slowly. Due to the rather long integration and preparation time of the VIPER, pauses are crucial to measure water properties at individual depths. In addition, pausing several times increases the number of data points along the profile and improves the coverage of the water column. Additionally, each profile should include one VIPER measurement right below the ice and one at maximum depth of the profile.

These considerations concerning the VIPER cast also enhance the options to investigate the optical properties of the water column with spectral analysis. Spectral extinction coefficients estimated along the profile from the RAMSES radiometers are not usable due to a small signal to noise ratio in deeper layers. Therefore, the spectral analysis has to rely on VIPER data.

It is therefore suggested that future depth profiles consist of one RAMSES cast and one VIPER cast. As both casts sample the same water column, a comparison is still possible afterwards. Furthermore, it is important to have the same routines for each profile at every individual station. The time required to cover similar distances needs to be the same for each individual station in order to make them comparable. Given the influence mixing has on the upcast beam attenuation spectra of the VIPER, downcast profiles should

focus on VIPER measurements, while RAMSES measurements are conducted during the upcasts.

Given the fact that the available data sets are not yet sufficient for the intended analysis, it is necessary to increase the number of depth profiles at individual stations in addition to the above mentioned suggestions. Subsequently, future analyses would be provided with additional RAMSES and VIPER data to validate findings.

6.3 Conclusion

The changes in Arctic sea-ice cover associated with current climate change increase the light availability in the Arctic ocean. A detailed examination of the vertical partitioning of this unprecedented energy input is crucial for understanding the consequences of current changes. Considering the current reduction of Arctic sea ice, significant alterations of the Arctic Ocean environment are expected. Unfortunately, data limitations hindered the intended analysis significantly. The PS101 campaign was the first field campaign for the newly acquired ROV system. In order to operate the ROV and its sensors to their full potential, it has to be acknowledged that the system is still undergoing extensive trials. Without these tests a sufficiently high data quality can not be ensured. Due to the prevailing conditions in the polar environment, part of this required test phase has to be conducted in the field.

Hence, instead of identifying optically different layers in the water column below Arctic sea ice, the focus of this analysis shifted to searching for potential improvements of the system and its measurement techniques. Current findings contributed to the preparation process of the second field campaign with the new ROV system (PS106, May 24 to July 20, 2017). Considerations concerning the improvement of ROV routines during depth profiles were applied during this expedition. In addition, the insights into the measurement constraints of the VIPER extinction sensor led to a change in the instrument setup. The optical path length was extended (from $0.15\,\mathrm{m}$ to $0.25\,\mathrm{m}$) in order to lower the detection minimum of the sensor from 0.1535 to $0.0921\,m^{-1}$. This path length extension adjusts the instrument to the clear water conditions of the designated sample area.

The presented analysis of the first available data set is an important step towards identifying advantages and deficiencies of the system. However, developing and improving the ROV and its instruments remains a process. Hence, further campaigns are necessary to improve the measurement and data processing techniques before a reliable investigation of layers with distinct optical properties along depth profiles in the Arctic is achievable.

Acknowledgements

First of all, I would like to thank Dr. Christian Katlein and Dr. Marcel Nicolaus for taking me on the PS92 cruise in 2015 and keeping me around to continue to work with the ROV. Working with you after PS92 led to this thesis and I am extremely grateful for the opportunity you gave me. Furthermore, I would like to thank you for your support and comments during the process of writing this thesis.

I would also like to thank Prof. Dr. Katja Matthes for agreeing to be my first supervisor and for encouraging me to write this thesis at AWI. Also, thank you again for allowing me to change the schedule multiple times during this thesis.

A very special thanks to Steffi Arndt for a very, very long list of things. Most importantly, for being a great friend and for always being straight with me. Thank you!

Katherine Turner, thank you for your friendship. If there is ever someone who is surprised that this thesis is written by a German, it is because of you!

Thank you to the Sea Ice Physics group. You guys let me sleep at your apartment, distracted me when it was necessary and took me in as an equal member of the group. I appreciate that and look forward to working with you!

Finally, I want to thank my parents. You know what you did. This is for you. I love you!

References

Arndt, S.: Sea-ice surface properties and their impact on the under-ice light field from remote sensing data and in-situ measurements, Ph.D. thesis, University Bremen, 2016.

AWI: Press release: Offenes Wasser um den Nordpol: Arktisches Meereis auf dem Rückzug., AWI, University Hamburg and CEN-Centre, 2016.

Belzile, C., Johannessen, S. C., Gosselin, M., Demers, S., and Miller, W. L.: Ultraviolet attenuation by dissolved and particulate constituents of first-year ice during late spring in an Arctic polynya, Limnology and Oceanography, 45, 1265–1273, 2000.

Boetius, A.: The Expedition PS101 of the Research Vessel POLARSTERN to the Arctic Ocean in 2016, no. 706 in Report on Polar and Marine Research, AWI, Alfred-Wegener-Institut Helmholtz-Zentrum für Polar- und Meeresforschung, Am Handelshafen 12, 27570 Bremerhaven, Germany, 2017.

Brandon, M. A., Cottier, F. R., and Nilsen, F.: Sea ice and Oceanography, Wiley-Blackwell, second edn., 2010.

Bricaud, A., Babin, M., Morel, A., and Claustre, H.: Variability in the chlorophyll-specific absorption coefficients of natural phytoplankton: Analysis and parametrization, Journal of Geophysical Research, 100, 13 321–13 332, 1995.

Cavalieri, D. J. and Parkinson, C. L.: Arctic sea ice variability and trends, 1979-2010, Cryosphere, pp. 957–979, 2012.

Clark, D. B., Feddersen, F., Omand, M. M., and Guza, R. T.: Measuring Fluorescent Dye in the Bubbly and Sediment-Laden Surfzone, Water, Air and Soil Pollution, 204, 103–115, 2009.

Comiso, J. C.: Polar Oceans from Space, Springer Science and Business Media, 2010.

Comiso, J. C. and Nishio, F.: Trends in the sea ice cover using enhanced and compatible AMSR-E, SSM/I and SMMR data, Journal of Geophysical Research: Oceans, 2008.

Dieckmann, G. S. and Hellmer, H. H.: The Importance of Sea Ice: An overview, Wiley-Blackwell, second edn., 2010.

Eicken, H., Gradinger, R., Salganek, M., Shirasawa, K., Perovich, D., and Leppaeranta, M.: Field Techniques for Sea Ice Research, University of Alaska Press, P.O. Box 756240, Fairbanks, AK, 2009.

Frey, K. E., Perovich, D. K., and Light, B.: The spatial distribution of solar radiation under a melting Arctic sea ice cover, Geophysical Research Letters, 38, 2011.

Grenfell, T. C. and Maykut, G. A.: The Optical Properties of Ice and Snow in the Arctic Basin, Journal of Glaciology, 18, 445–463, 1977.

Haas, C.: Dynamic Versus Thermodynamics: The Sea Ice Thickness Distribution, Wiley-Blackwell, second edn., 2010.

IPCC: Climate Change 2013: The Physical Science Basis. Contribution of Working Group I to the Fifth Assessment Report of the Intergovernmental Panel on Climate Change, Cambridge University Press, Cambridge, UK and New York, NY, USA, 2013.

Katlein, C., Arndt, S., Nicolaus, M., Perovich, D. K., Jakuba, M. V., Suman, S., Elliot, S., Whitcomb, L. L., McFarland, C. J., Gerdes, R., Boetius, A., and German, C. R.: Influence of ice thickness and surface properties on light transmission through Arctic sea ice, Journal of Geophysical Research: Ocean, 2015.

Katlein, C., Perovich, D. K., and Nicolaus, M.: Geometric Effects of an Inhomogeneous Sea Ice Cover on the under Ice Light Field, FRONTIERS in Earth Science, 2016.

Katlein, C., Schiller, M., Belter, H. J., Coppolaro, V., Wenslandt, D., and Nicolaus, M.: A new remotely operated sensor platform for interdisciplinary observations under sea ice, FRONTIERS in Earth Science, in review, submitted.

Kwok, R. and Rothrock, D. A.: Decline in Arctic sea ice thickness from submarine and ICESat records: 1958-2008, Geophysical Research Letters, 36, 2009.

Laney, S. R., Krishfield, R. A., Toole, J. M., Hammar, T. R., Ashjian, C. J., and Timmermans, M.-L.: Assessing algal biomass and bio-optical distributions in perennially ice-covered polar ocean ecosystems, Polar Science, 8, 73–85, 2014.

Laney, S. R., Krishfield, R. A., and Toole, J. M.: The euphotic zone under Arctic Ocean sea ice: Vertical extents and seasonal trends, Limnology and Oceanography, 2017.

Light, B., Grenfell, T. C., and Perovich, D. K.: Transmission and absorption of solar radiation by Arctic sea ice during the melt season, Journal of Geophysical Research: Oceans, 113, 2008.

Liou, K. N.: An Introduction to Atmospheric Radiation, Academic Press, ELSEVIER Science, second edn., 2002.

Maslanik, J. A., Fowler, C., Stroeve, J., Drobot, S., Zwally, J., Yi, D., and Emery, W.: A younger, thinner Arctic ice cover: Increased potential for rapid, extensive sea-ice loss, Geophysical Research Letters, 34, 2007.

Mobley, C., Boss, E., and Roesler, C.: Ocean Optics Web Book, http://www.oceanopticsbook.info/view/introduction/overview, 2016.

Nicolaus, M. and Katlein, C.: Mapping radiation transfer through sea ice using a remotely operated vehicle (ROV), The Cryosphere, pp. 763–777, 2013.

Nicolaus, M., Gerland, S., Hudson, S. R., Hanson, S., Haapala, J., and Perovich, D. K.: Seasonality of spectral albedo and transmittance observed in the Arctic Transpolar Drift in 2007., Journal of Geophysical Research, 115, 2010a.

Nicolaus, M., Hudson, S. R., Gerland, S., and Munderloh, K.: A modern concept for autonomous and continuous measurments of spectral albedo and transmittance of sea ice, Cold Regions Science and Technology, pp. 14 – 28, 2010b.

Nicolaus, M., Katlein, C., Maslanik, J., and Hendricks, S.: Changes in Arctic sea ice result in increasing light transmittance and absorption, Geophysical Research Letters, 39, 2012.

Perovich, D. K.: The Optical Properties of Sea Ice, Cold Regions Research and Engineering Laboratory, 1, 1996.

Perovich, D. K. and Richter-Menge, J. A.: Loss of Sea Ice in the Arctic, The Annual Review of Marine Science, pp. 417–441, 2009.

Persson, P. O. G., Fairall, C. W., Andreas, E. L., Guest, P. S., and Perovich, D. K.: Measurements near the Atmospheric Surface Flux Group tower at SHEBA: Near-surface conditions and surface energy budget, Journal of Geophysical Research, 107, 2002.

Petrich, C. and Eicken, H.: Growth, Structure and Properties of Sea Ice, Wiley-Blackwell, second edn., 2010.

Petrich, C., Nicolaus, M., and Gradinger, R.: Sensitivity of the light field under sea ice to inhomogeneous optical properties and incident light assessed with three-dimensional Monte Carlo radiative transfer simulations, Cold Regions Science and Technology, pp. 1–11, 2012.

Ramirez-Perez, M., Torrecilla, E., Sanchez, A. M., and Piera, J.: Do hyperspectral transmissometers allow us to go one step further on the analysis of particulate matter characteristics of marine samples?, OCEANS 2014-Taipei. IEEE, pp. 1–5, 2014.

Sturm, M. and Massom, R. A.: Snow and Sea Ice, Wiley-Blackwell, second edn., 2010.

Taskjelle, T., Granskog, M. A., Pavlov, A. K., Hudson, S. R., and Hamre, B.: Effects of an Arctic under-ice bloom on solar radiant heating of the water column, Journal of Geophysical Research: Oceans, 122, 2016.

Thomas, D. N. and Dieckmann, G. S.: Glossary, Wiley-Blackwell, 2010.

TriOS: Radiometers RAMSES, TriOS Mess- und Datentechnik GmbH, Buergermeister-Broetje-Str. 25, 26180 Rastede, Manual 2016.

TriOS: VIPER (Submersible VIS process spectrophotometer) manual (2016), TriOS Mess- und Datentechnik GmbH, Buergermeister-Broetje-Str. 25, 26180 Rastede, preliminary manual.

Untersteiner, N.: The Geophysics of Sea Ice, vol. 146 of B, NATO Advanced Science Institutes Series, Springer, University of Washington, 1981.

Vaughan, D. G., Comiso, J. C., Allison, I., Carrasco, J., Kaser, G., Kwok, R., Mote, P., Murray, T., Paul, F., Ren, J., Rignot, E., Solomina, O., Steffen, K., and Zhang, T.: Observations: Cryosphere. In Climate Change 2013: The Physical Science Basis. Contribution of Working Group I to the Fifth Assessment Report of the Intergovernmental Panel on Climate Change, Cambridge University Press, Cambridge, UK and New York, NY, USA, 2013.

von Storch, H. and Zwiers, F. W.: Statistical Analysis in Climate Research, Cambridge University Press (Virtual Publishing), 2003.

WETLabs: ECO Fluorometers and Scattering Sensors, WETLabs, Manual 2016.

Appendix

A.1 Additional figures

A.1.1 Exponential fitting (RAMSES)
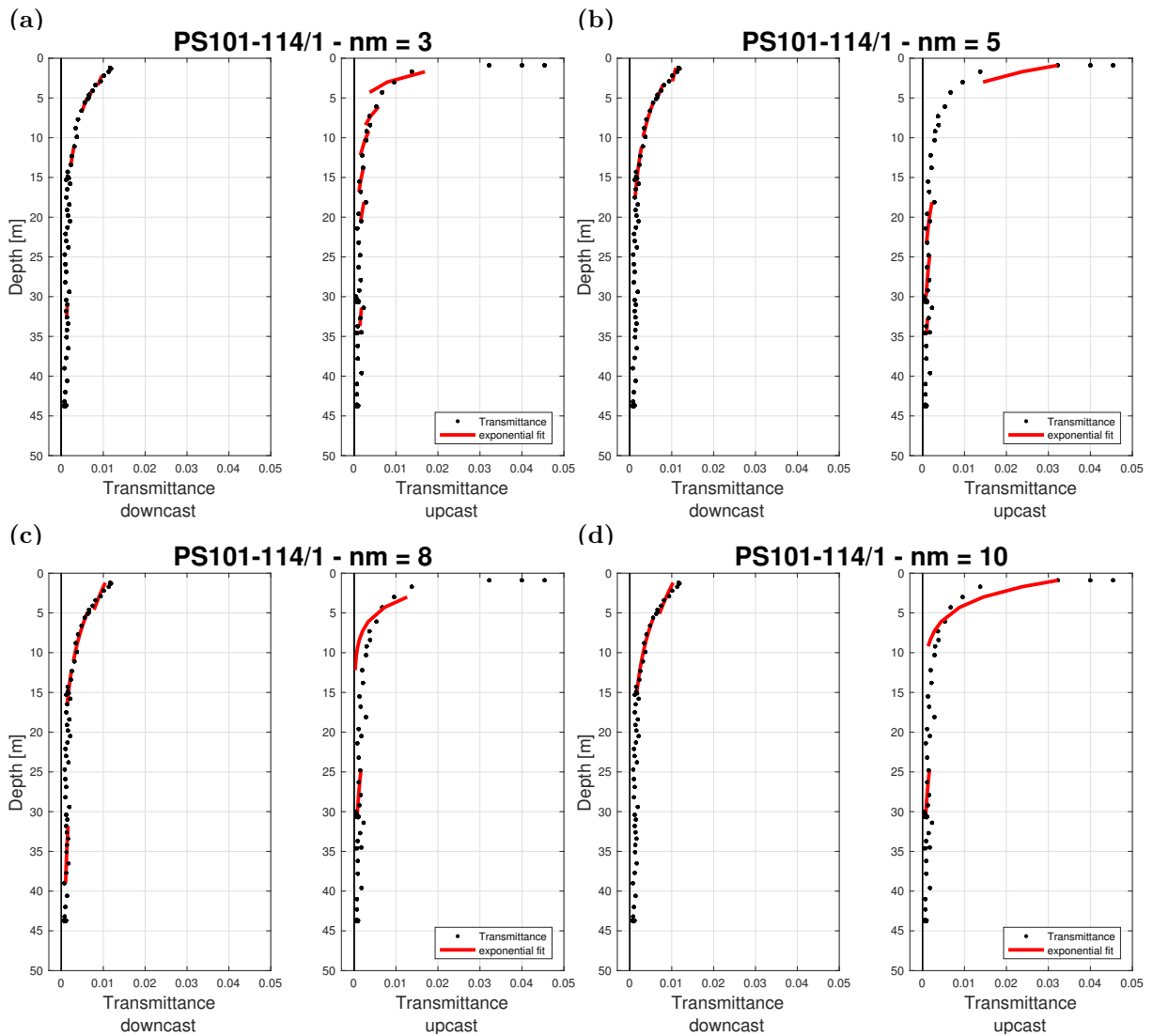
Multi-layer fitting (PS101-114)

Figure A.1: Multiple fitting approach using a predefined number of consecutive data points (*nm*) for each fit along the depth profile of station PS101-114. *Left* panels show calculated transmittance values (*black* dots) during the downcast, *right* panels during the upcast, respectively. *Red* lines indicate the exponential fits for the scenarios (a) *nm*3, (b) *nm*5, (c) *nm*8 and (d) *nm*10.
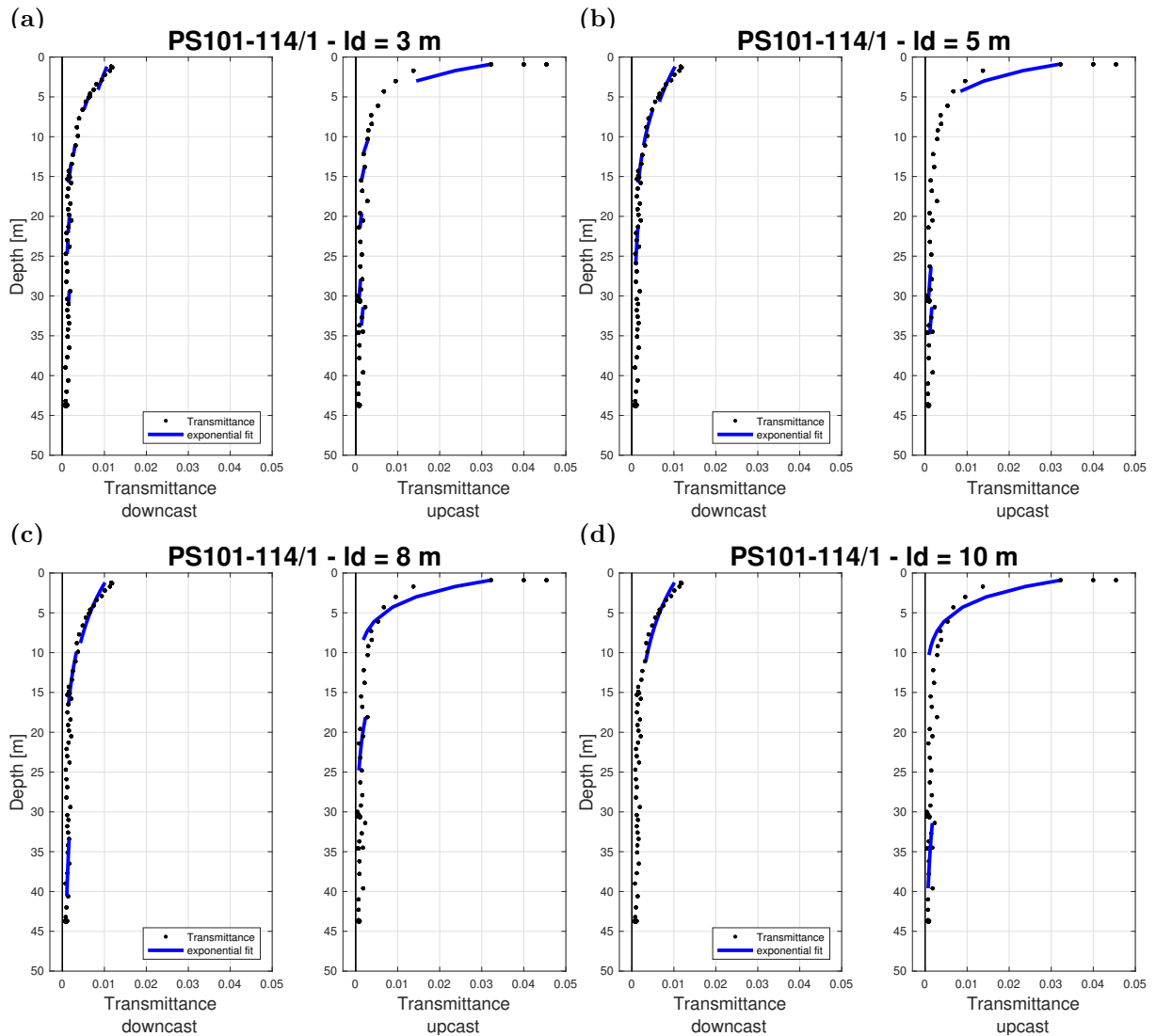
Figure A.2: Multiple fitting approach using a predefined layer of the thickness (ld) for each fit along the depth profile of station PS101-114. *Left* panels show calculated transmittance values (*black* dots) during the downcast, *right* panels during the upcast, respectively. *Blue* lines indicate the exponential fits for the scenarios (a) $ld3$, (b) $ld5$, (c) $ld8$ and (d) $ld10$.

A.1.2 RAMSES versus VIPER (PS101-142)

(a)
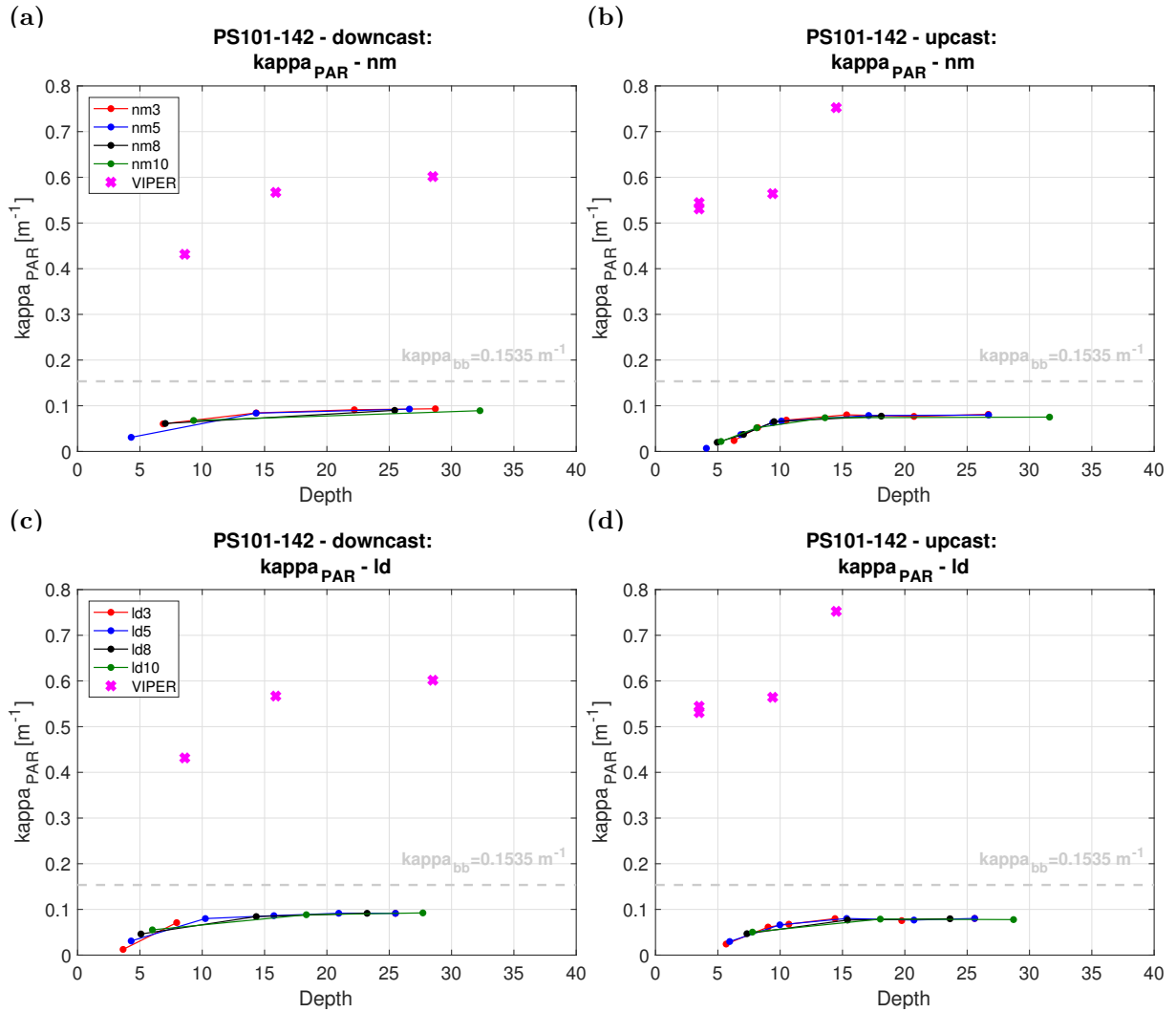

(b)

(c)

(d)

Figure A.3: PAR extinction coefficients calculated from the RAMSES and VIPER (x-markers) data for station PS101-142. RAMSES PAR extinction coefficients are estimated using the *nm*-method (panels (a) and (b)) and the *ld*-method (panels (c) and (d)). Panels (a) and (c) show downcast values, while (c) and (d) give upcast values. *Red* dots indicate the *nm*3/*ld*3 scenario, *blue* shows *nm*5/*ld*5, *black* the *nm*8/*ld*8 and *green* the *nm*10/*ld*10 results. The dotted *grey* line indicates the minimum broadband extinction coefficient detectable with the current VIPER setup (optical path length: 0.15 m).

Statement/Erklärung

I hereby declare that I have written this thesis on my own and that I have used no other than the cited and mentioned sources and aids. The submitted printed version is equivalent to the data file on the electronic medium.

Filename: BELTER_5686.pdf

Finally, I affirm that this work has not been submitted for any other degree.

Hiermit erkläre ich, dass ich diese Masterarbeit selbstständig und nur mit Hilfe der angegeben Referenzen und Hilfsmittel angefertig habe. Die eingereichte Version stimmt mit der auf dem elektronischen Speichermedium überein.

Dateiname: BELTER_5686.pdf

Weiter bestätige ich, dass ich diese Arbeit noch nicht für einen Abschluss an anderer Stelle eingereicht habe.

Bremerhaven, July 27, 2017   Hans JAKOB Belter